J. Fluid Mech. (2012), *vol.* 704, *pp.* 251–279. © Cambridge University Press 2012
doi:10.1017/jfm.2012.235

Spatial optimal growth in three-dimensional compressible boundary layers

David Tempelmann[1]†, Ardeshir Hanifi[1,2] and Dan S. Henningson[1]

[1] Linné Flow Center, SeRC, KTH Mechanics, SE-100 44 Stockholm, Sweden
[2] Swedish Defence Research Agency, FOI, SE-164 90 Stockholm, Sweden

(Received 22 July 2011; revised 28 February 2012; accepted 15 May 2012;
first published online 2 July 2012)

This paper represents a continuation of the work by Tempelmann *et al.* (*J. Fluid Mech.*, vol. 646, 2010*b*, pp. 5–37) on spatial optimal growth in incompressible boundary layers over swept flat plates. We present an extension of the methodology to compressible flow. Also, we account for curvature effects. Spatial optimal growth is studied for boundary layers over both flat and curved swept plates with adiabatic and cooled walls. We find that optimal growth increases for higher Mach numbers. In general, extensive non-modal growth is observed for all boundary layer cases even in subcritical regions, i.e. where the flow is stable with respect to modal crossflow disturbances. Wall cooling, despite stabilizing crossflow modes, destabilizes disturbances of non-modal nature. Curvature acts similarly on modal as well as non-modal disturbances. Convex walls have a stabilizing effect on the boundary layer whereas concave walls have a destabilizing effect. The physical mechanisms of optimal growth in all studied boundary layers are found to be similar to those identified for incompressible flat-plate boundary layers.

Key words: compressible boundary layers, boundary layer stability, boundary layer receptivity

1. Introduction

The transition process in boundary layers is mainly characterized by three stages: receptivity, growth and breakdown of disturbances. Receptivity is associated with the generation of disturbances inside a boundary layer which is exposed to an external disturbance environment. The excited disturbances grow while travelling downstream. At some position nonlinear effects become dominant and lead to a rapid breakdown to turbulent flow. A number of experiments by Bippes and coworkers showed that the external disturbance environment determines the transition scenario in three-dimensional boundary layers (see Bippes 1999). High levels of free-stream turbulence, on the one hand, lead to transition scenarios dominated by non-stationary disturbances. Rough walls in combination with low levels of free-stream turbulence, on the other hand, lead to a disturbance environment which is dominated by stationary disturbances, although these grow in general less than their non-stationary counterparts. A complete and robust model of the transition process should therefore incorporate all three stages. However, semi-empirical transition prediction tools, which are in common use today, are based on the linear amplification of modal disturbances only. The

† Email address for correspondence: david@mech.kth.se

https://doi.org/10.1017/jfm.2012.235 Published online by Cambridge University Press

method presented in this study is part of the effort to include receptivity in transition modelling.

In terms of receptivity it makes sense to consider the worst-case scenario if the external disturbance field is not known (see Bottaro 2010). This implies finding those initial disturbances which experience maximum amplification, the so-called optimal disturbances. These have been studied extensively in the past for two-dimensional boundary layers, where they take the form of either streaks or Tollmien–Schlichting (TS) waves. The latter disturbances are of modal nature, i.e. they can be found as eigenmodes of the governing stability operator and grow exponentially. The former appear under conditions where TS waves are stable and are mathematically associated with the non-orthogonality of the governing operator. Accordingly, they are referred to as disturbances of non-modal nature. The physical mechanism responsible for non-modal growth is the well-known lift-up effect, which was outlined first by Landahl (1980). However, this algebraic, inviscid instability mechanism had originally been identified by Ellingsen & Palm (1975) for inviscid channel flow. Temporal non-modal growth in incompressible two-dimensional shear flows has been the subject of numerous studies, amongst others by Butler & Farrell (1992), Reddy & Henningson (1993) and Trefethen *et al.* (1993). The first spatial analyses of non-modal growth in a Blasius boundary layer were presented by Andersson, Berggren & Henningson (1999) and Luchini (2000), employing a parabolic set of perturbation equations derived on the basis of the boundary layer approximation.

The first study of non-modal growth in two-dimensional boundary layers that comprised effects of compressibility was performed by Hanifi, Schmid & Henningson (1996). These authors employed the temporal framework. They found non-modal growth to increase with increasing Mach numbers and to scale with the Reynolds number squared as in the incompressible case. This scaling was later verified analytically by Hanifi & Henningson (1998). The similarities between compressible and incompressible cases led to the conclusion that both exhibit the same physical mechanism of non-modal growth, i.e. the lift-up effect. The first spatial analysis of non-modal growth in compressible two-dimensional boundary layers was performed by Tumin & Reshotko (2001) assuming locally parallel flow. Non-parallel effects were later accounted for by Tumin & Reshotko (2003) and Zuccher, Tumin & Reshotko (2006). These studies also considered effects of wall cooling. It was concluded that the wall temperature affects the disturbance temperature profiles and destabilizes the flow with respect to non-modal growth. This is an interesting result since it is known that modal disturbances such as TS waves are damped by cooling the wall (see e.g. Mack 1984). On the basis of modal analysis, wall cooling would therefore represent a promising control mechanism in order to move the transition of boundary layers from laminar to turbulent flow further downstream. However, despite damping TS waves, wall cooling could move transition upstream by enhancing initial non-modal growth.

Effects of concave curvature on optimal growth have been studied by Cossu *et al.* (2000). They computed spatial optimal disturbances in a two-dimensional incompressible boundary layer on a concave wall. They observed initial disturbance growth of non-modal nature. However, the growth was sustained further downstream because of the existence of Görtler instabilities. The effects of convex curvature on non-modal growth in compressible two-dimensional boundary layers have been exploited by Reshotko & Tumin (2004*a*), studying optimal growth in the boundary layer over a sphere, and by Reshotko & Tumin (2004*b*), computing the optimal growth of a stagnation point flow. Their conclusion was that increasing convex curvature acts to stabilize non-modal growth.

https://doi.org/10.1017/jfm.2012.235 Published online by Cambridge University Press

Rather little work on non-modal and optimal disturbance growth has been performed for three-dimensional boundary layers. Employing a temporal approach, both Breuer & Kuraishi (1994) and Corbett & Bottaro (2001) showed that three-dimensional boundary layers also exhibit substantial non-modal growth. The disturbances subject to non-modal growth were found to be structurally similar to modal crossflow instabilities, which is in contrast to the two-dimensional case where streaks and TS waves bear no resemblance. This led to the conclusion by Corbett & Bottaro (2001) that non-modal growth provides the proper initial conditions for subsequent growth of modal disturbances, and may thus be related to a receptivity mechanism in three-dimensional boundary layers. To describe this process, i.e. the initiation of modal instabilities by non-modal growth, a spatial framework is needed, and was introduced by Tempelmann, Hanifi & Henningson (2010*b*) for incompressible three-dimensional boundary layers. They showed that optimal disturbances in the supercritical domain of a three-dimensional boundary layer are eventually represented by crossflow modes. However, initially these disturbances are of non-modal nature, experiencing strong growth. Further downstream each optimal disturbance turns into one corresponding exponentially growing crossflow mode. This mechanism resembles the one identified by Cossu *et al.* (2000) in the Görtler case.

In the following we extend the approach by Tempelmann *et al.* (2010*b*) to compressible three-dimensional boundary layer flows and investigate the effects of compressibility, wall cooling and both concave and convex wall curvature on optimal disturbance growth. It should be noted that, in boundary layers of practical interest such as on swept wings, we do not expect the worst-case scenarios studied here to occur. However, the computation of optimal disturbances in a linear spatial framework allows us to study the potential of a certain boundary layer for non-modal growth and thus possible receptivity mechanisms. Many external disturbances such as free-stream turbulence or surface roughness can generate disturbances of similar shape as compared to the optimal ones. Hence, the more potential a boundary layer has for non-modal growth the more receptive it might be to specific external disturbances. Furthermore, optimal disturbances can be used directly for receptivity predictions by projecting external disturbances onto an orthogonal set of disturbances comprising the optimal disturbance and several sub-optimal disturbances. For a detailed description of this approach the reader is referred to Tempelmann, Hanifi & Henningson (2010*a*).

The methodology which is adopted in the following to compute optimal disturbances is similar to that developed by Tempelmann *et al.* (2010*a*,*b*), and is based on the linear parabolized stability equations (PSEs) originally introduced by Herbert & Bertolotti and Dallmann & Simen (see e.g. Bertolotti, Herbert & Spalart 1992; Simen 1992).

2. Methodology

2.1. *Governing equations*

Our intention is to find a set of linear governing equations that is parabolic in nature. Such a system can be solved efficiently by employing marching techniques, and allows for extensive parametric studies. It is derived from the continuity, momentum and energy equations for compressible flow by decomposing all flow quantities into a mean and a perturbation part, by subtracting the equations describing the meanflow and by neglecting products of perturbation quantities. We then assume disturbances

https://doi.org/10.1017/jfm.2012.235 Published online by Cambridge University Press

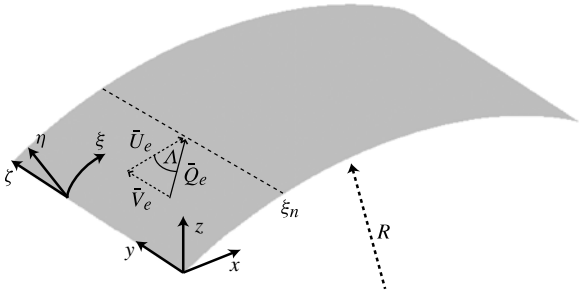


FIGURE 1. The flow case studied is a swept plate with a sweep angle of $\Lambda = 45°$. The radius of curvature is represented by R. The orthogonal, curvilinear coordinate system is denoted by (ξ, ζ, η) and will coincide with the Cartesian coordinates (x, y, z) for $R = \infty$. Velocity components in (ξ, ζ, η)-directions are denoted by (u, v, w). $\bar{Q}$ denotes the meanflow velocity in the direction of the outer streamline. Quantities at the boundary layer edge are denoted by the subscript 'e' and ξ_n is a reference position defined in § 3.

of the form

$$\Phi'(\xi, \zeta, \eta, t) = \Phi(\xi, \eta) \exp \mathrm{i} \left(\int_{\xi_0}^{\xi} \alpha(\xi') \, \mathrm{d}\xi' + \beta\zeta - \omega t \right) + \text{c.c.} \tag{2.1}$$

where Φ represents any of the disturbance components $[\rho, u, v, w, T, p]$ and c.c. denotes the complex conjugate. The orthogonal curvilinear coordinate system is defined by (ξ, ζ, η), denoting the tangential, spanwise and wall-normal directions (see figure 1), and (u, v, w) represent the corresponding velocity components.

The subscript '0' denotes the initial position. The disturbance density is denoted by ρ whereas T represents the disturbance temperature. The wavenumbers (α, β) are associated with the respective tangential and spanwise directions (ξ, ζ) and the radial frequency is represented by ω. Further, we introduce the scaling parameter $\epsilon = \delta/L = Re^{-1/2}$, where $Re = Q_{ref} L/\nu$ denotes the Reynolds number, with ν being the kinematic viscosity and Q_{ref} representing a characteristic reference velocity. Here, $\delta = \sqrt{\nu L/Q_{ref}}$ and L represent characteristic length scales in the η- and ξ-directions respectively, and $\delta \ll L$. Following the derivation of the parabolized stability equations by Hanifi *et al.* (1994), we assume that the shape function $\boldsymbol{q}$ and the wavenumber α are slowly varying in ξ. We therefore normalize ξ with L whereas η is normalized with $\epsilon L = \delta$. The disturbance velocity components (u, v, w) are scaled with $(Q_{ref}, Q_{ref}, Q_{ref})$. Note that the respective meanflow velocity components are assumed to scale with $(Q_{ref}, Q_{ref}, \epsilon Q_{ref})$. Further, the disturbance pressure is made non-dimensional with $\rho_{ref} Q_{ref}^2$ while the temperature T is normalized with T_{ref}. The density ρ is related to pressure and temperature through the state equation. The wavenumbers (α, β) are both scaled with $1/\epsilon L = 1/\delta$. Introducing these scalings and ansatz (2.1) into the linearized disturbance equations and neglecting terms which are of order $O(\epsilon^2)$ and higher, we arrive at a parabolized set of equations of the form

$$\boldsymbol{A}\boldsymbol{q} + \boldsymbol{B}\frac{\partial \boldsymbol{q}}{\partial \eta} + \boldsymbol{C}\frac{\partial^2 \boldsymbol{q}}{\partial \eta^2} + \boldsymbol{D}\frac{1}{h_1}\frac{\partial \boldsymbol{q}}{\partial \xi} = 0, \tag{2.2}$$

where $\boldsymbol{q} = (\rho, u, v, w, T)^{\mathrm{T}}$. The disturbance pressure is eliminated using the equation of state. Note that the system (2.2) is only quasi-parabolic (see Haj-Hariri 1994; Andersson, Henningson & Hanifi 1998). Upstream travelling acoustic waves may lead

https://doi.org/10.1017/jfm.2012.235 Published online by Cambridge University Press

to numerical instabilities at small $\delta\xi$. We neglect the disturbance pressure gradient $\partial p/\partial\xi$ in the following to avoid such numerical instabilities. Numerous numerical tests (see e.g. § 4) and results by Tempelmann *et al.* (2010*b*) showed that $\partial p/\partial\xi$ is indeed of higher order and thus negligible for crossflow-dominated swept-plate boundary layers. Further justification is given by Tempelmann (2009), who compared results from nonlinear PSE computations to experiments of a three-dimensional flat-plate boundary layer by Kurian, Fransson & Alfredsson (2011). A perfect match could only be obtained by neglecting the chordwise pressure gradient to allow for sufficient resolution.

The linear operators $\boldsymbol{A}$, $\boldsymbol{B}$, $\boldsymbol{C}$ and $\boldsymbol{D}$ can be obtained from Pralits *et al.* (2000) if $\partial p/\partial\xi$ is eliminated from the ξ-momentum equation. The scaling factor that arises because of the orthogonal curvilinear metric is defined as $h_1^2 = \sum_{j=1}^{3} (\partial x_j/\partial\xi)^2$, where x_j represents the Cartesian coordinates (x, y, z) of the reference system. The Dirichlet boundary conditions $(u, v, w, T) = 0$ are imposed at the wall and in the free stream. The first coefficient of viscosity, μ, is determined from a combination of Sutherland's formula and a linear relation given by Mack (1965). The second coefficient of viscosity, λ, is obtained on the basis of Stokes' hypothesis. The latter implies the assumption of zero bulk viscosity which is generally true only for dilute monatomic gases (for a review see Graves & Arrow 1999). However, it is very difficult to accurately determine the second viscosity coefficient from experiments (for details see Flügge & Tresdell 1959; Graves & Arrow 1999) and therefore many studies of compressible flow employ Stokes' hypothesis. When studying the stability of compressible boundary layers it was found that the choice of λ is important for second-mode instabilities. However, for first-mode instabilities its influence is negligible (see e.g. Kufner 1995). In appendix A we show that this is also true for the crossflow disturbances studied in this article and we therefore use Stokes' hypothesis in the following. Finally, we assume constant specific heat, c_p, and a constant Prandtl number, which then define the thermal conductivity κ.

In order to be able to solve (2.2) we need to resolve the ambiguity that both $\boldsymbol{q}$ and α are functions of ξ. We do this by choosing α to be the real-valued wavenumber such that all the periodic oscillations of Φ' are captured by the exponential part of (2.1). All the disturbance growth is then captured by the shape function $\boldsymbol{q}$. The tangential component of the physical wavevector is given by Bertolotti & Herbert (1991) and Hanifi *et al.* (1994) as $\alpha_{ph} = \tilde{\alpha}/h_1$, where $\tilde{\alpha}$ is defined by

$$\tilde{\alpha} = \mathrm{Re}(\alpha) + \mathrm{Im}\left(\frac{1}{A}\frac{\partial A}{\partial\xi}\right). \tag{2.3}$$

Re and Im represent real and imaginary parts of a complex number and $A(\xi)$ represents a complex amplitude such that $\boldsymbol{q}(\xi, \eta) = A(\xi)\hat{\boldsymbol{q}}(\xi, \eta)$. Here, $\hat{\boldsymbol{q}}$ denotes the normalized disturbance quantities. There is no unique choice for $A(\xi)$, but in the following we choose $A(\xi) = \max_\eta(u_{cp})$. In this study we expect to find disturbance environments inside the boundary layer which are dominated by crossflow vortices and streaky disturbances. Hence u_{cp}, the disturbance velocity component tangential to the line of constant phase, is a reasonable choice. Requiring all periodic oscillations of Φ' to be captured by the exponential part implies $\mathrm{Im}(1/A\partial A/\partial\xi) = 0$. In practice the latter condition can be satisfied approximately by determining α iteratively using (2.3). We start with an initial guess for α on the basis of the observation that disturbances are closely aligned with the outer streamline in crossflow-dominated boundary layers.

https://doi.org/10.1017/jfm.2012.235 Published online by Cambridge University Press

In the next iteration step we set $\alpha = \tilde{\alpha}$. The latter step is repeated until the energy growth has converged. The methods used by Tempelmann *et al.* (2010*a*,*b*) are identical but described from a different viewpoint.

2.2. *Optimality system*

We want to compute the optimal disturbance $\boldsymbol{q}$ that experiences maximum energy amplification at a specific position ξ_1. This means that we want to maximize the objective function

$$J(\boldsymbol{q}) = \frac{E(\xi_1)}{E(\xi_0)}, \tag{2.4}$$

where E denotes the norm of $\boldsymbol{q}$ measuring the size of the disturbance and ξ_0 denotes the initial position. However, the choice of norm is not obvious in this case. Ting (1965) outlines that only three out of five variables can be prescribed as an initial condition at the inflow when solving the two-dimensional compressible boundary layer equations. This is because of the existence of a compatibility equation which relates the variables $\bar{\rho}, \bar{u}$ and $\bar{w}$ with each other. Based on that conclusion and on the observation by Luchini (2000) that the optimal disturbance in a two-dimensional, incompressible boundary layer has $u = p = 0$ at $\xi = 0$, Zuccher *et al.* (2006) consider initial disturbances with only v and w non-zero. However, they admit that this does not generally guarantee the largest energy gain in the compressible case.

In the more general three-dimensional case things are different. First of all no compatibility equation can be derived for (2.2). Hence, all five variables need to be prescribed initially. Further, we know from Tempelmann *et al.* (2010*b*) that the largest gain in a three-dimensional incompressible boundary layer is obtained when all three velocity components are considered. Here, we want to use a norm that measures the size of the disturbance based on all five state variables. A positive definite energy norm which is appropriate in the compressible case, and which we will use in the following, has been derived by Mack (1969) and Hanifi *et al.* (1996). It has the form

$$E(\xi) = \int_0^\infty \boldsymbol{q}\,(\xi)^{\mathrm{H}}\, \boldsymbol{M}\boldsymbol{q}(\xi)\,\mathrm{d}\eta, \tag{2.5}$$

where the energy weight matrix is defined by

$$\boldsymbol{M} = \mathrm{diag}\left[\frac{\bar{T}(\xi)}{\bar{\rho}(\xi)\gamma M^2}, \bar{\rho}(\xi), \bar{\rho}(\xi), \bar{\rho}(\xi), \frac{\bar{\rho}(\xi)}{\gamma(\gamma-1)\bar{T}(\xi)M^2}\right]. \tag{2.6}$$

An overbar denotes meanflow quantities, γ is the specific heat ratio and M is the Mach number. Note that (2.6) was derived for the temporal case where pressure-related terms in the energy evolution equation cancel. Hence, compression work, which is conservative, is not accounted for. However, in the spatial case this norm is postulated. In order to show how sensitive results are to different norms, e.g. those which do not account for all state variables, we show one parametric study in appendix B where the kinetic energy is used. Apart from appendix B, (2.6) is used as a norm in the following. In order to find the disturbance that maximizes $J(\boldsymbol{q})$, we construct a Lagrange functional

$$\mathscr{L}(\boldsymbol{q}, \boldsymbol{q}^\star) = J(\boldsymbol{q}) - \left(\int\int_\Omega (\boldsymbol{q}^\star)^{\mathrm{H}}\, \boldsymbol{L}\boldsymbol{q} h_1 \mathrm{d}\xi\,\mathrm{d}\eta + \mathrm{c.c.}\right). \tag{2.7}$$

https://doi.org/10.1017/jfm.2012.235 Published online by Cambridge University Press

Here, $\boldsymbol{Lq}$ represents the left-hand side of (2.2), $\boldsymbol{q}^\star = (\rho^\star, u^\star, v^\star, w^\star, T^\star)^{\mathrm{T}}$ is the Lagrange multiplier, which is also referred to as the adjoint variable, $\Omega = [\xi_0, \xi_1] \times [0, \infty]$ and the superscript 'H' denotes conjugate transpose. The roots of the first variation of (2.7), which becomes

$$\delta\mathscr{L} = \int\!\!\int_{\Omega} (\boldsymbol{\nabla}_{\boldsymbol{q}^\star}\mathscr{L})^{\mathrm{H}}\, \delta\boldsymbol{q}^\star h_1 \,\mathrm{d}\xi\,\mathrm{d}\eta + \int\!\!\int_{\Omega} (\boldsymbol{\nabla}_{\boldsymbol{q}}\mathscr{L})^{\mathrm{H}}\, \delta\boldsymbol{q} h_1 \,\mathrm{d}\xi\,\mathrm{d}\eta + \text{c.c.}, \tag{2.8}$$

will then represent the optimal disturbance and its corresponding adjoint. $\boldsymbol{\nabla}$ denotes a gradient, i.e. $\nabla_{\boldsymbol{q}}$ represents a gradient with respect to $\boldsymbol{q}$. To obtain these roots both inner products in (2.8) have to vanish independently. Setting the first inner product to zero implies solving (2.2), i.e. $\boldsymbol{Lq} = 0$. The second inner product will be zero if $\nabla_{\boldsymbol{q}}\mathscr{L} = 0$. This gradient is most easily obtained by using the identity

$$\int\!\!\int_{\Omega} (\boldsymbol{q}^\star)^{\mathrm{H}}\, \boldsymbol{L}\boldsymbol{q} h_1 \mathrm{d}\xi\,\mathrm{d}\eta = \int\!\!\int_{\Omega} (\boldsymbol{L}^\star\boldsymbol{q}^\star)^{\mathrm{H}}\, \boldsymbol{q} h_1 \mathrm{d}\xi\,\mathrm{d}\eta + \int_{\xi_0}^{\xi_1} \left[\boldsymbol{K}_\eta\right]_{\eta=0}^{\eta=\infty} \mathrm{d}\xi + \int_0^{\infty} [\boldsymbol{K}_\xi]_{\xi_0}^{\xi_1}\,\mathrm{d}\eta, \tag{2.9}$$

which is derived by employing integration by parts. The boundary terms represented by $\boldsymbol{K}_\eta$ vanish if we impose the boundary conditions $(u^\star, v^\star, w^\star, T^\star) = 0$ at the wall and in the free stream. Rendering the second inner product of (2.8) zero thus implies solving $\boldsymbol{L}^\star\boldsymbol{q}^\star = 0$, the so-called adjoint PSE, as well as satisfying the optimality conditions at ξ_0 and ξ_1. For a detailed derivation of the adjoint PSE the reader is referred to Pralits *et al.* (2000). The optimality condition results from the boundary terms $\boldsymbol{K}_\xi$ and the gradient of the objective function, $\nabla_{\boldsymbol{q}} J$, and is obtained from (2.9) as

$$\boldsymbol{D}^{\mathrm{H}}\boldsymbol{q}_k^\star - c_k\boldsymbol{M}\boldsymbol{q}_k = 0. \tag{2.10}$$

The subscript k denotes either ξ_0 or ξ_1, and c denotes a normalization coefficient. Condition (2.10) relates the solutions of the PSE (2.2) and the adjoint equations at ξ_0 and ξ_1 respectively. The initial condition of the adjoint equations at ξ_1 can be readily found from

$$\boldsymbol{q}_1^\star = (\boldsymbol{D}^{\mathrm{H}})^{-1}\, c_1\boldsymbol{M}_1\boldsymbol{q}_1. \tag{2.11}$$

Note that $\boldsymbol{D}^{\mathrm{H}}$ is singular at the wall and that the adjoint equations do not comprise boundary conditions for $\rho^\star$. Hence, to render (2.11) solvable we prescribe $\rho_1^\star$ at the wall. The boundary value of $\rho_1^\star$ at $\eta = 0$ is obtained from the third adjoint equation which, at the wall, relates $\rho^\star$ to all other adjoint state variables. The candidate optimal initial condition at ξ_0 is found accordingly from

$$\boldsymbol{q}_0 = \frac{1}{c_0}\,(\boldsymbol{M})^{-1}\,\boldsymbol{D}^{\mathrm{H}}\boldsymbol{q}^\star. \tag{2.12}$$

The optimality condition for $u(\xi_0)$ then becomes

$$u(\xi_0) = \rho^\star(\xi_0) + \bar{U}(\xi_0)u^\star(\xi_0). \tag{2.13}$$

Since $\rho^\star$ is non-zero at the wall, relation (2.13) would also yield a non-zero candidate optimal initial disturbance $u(\xi_0)$ at $\eta = 0$. A similar issue arises in the incompressible case, as outlined by Zuccher *et al.* (2006) and Tempelmann *et al.* (2010*b*). There are several ways to resolve this inconsistency. Zuccher *et al.* (2006) chose to smooth $u(\xi_0)$ close to the wall by fitting a polynomial satisfying the no-slip boundary conditions at the wall. Tempelmann *et al.* (2010*b*), who studied incompressible flow, neglected those

https://doi.org/10.1017/jfm.2012.235 Published online by Cambridge University Press

parts of a sum similar to (2.13) which did not satisfy the boundary conditions. Results obtained using this approach were compared to the optimal growth computed with the unmodified, unphysical candidate optimal initial disturbance. Results were identical, showing that the modification had a negligible effect on spatial optimal growth. Here, we follow Tempelmann *et al.* (2010*b*) and neglect $\rho^\star$ in (2.13) in order to make $u(\xi_0)$ satisfy the boundary conditions. The optimality system is solved iteratively as described in Tempelmann *et al.* (2010*b*).

2.3. *Global optimization*

The solution to the optimality system described above is the initial disturbance $\boldsymbol{q}_0$ yielding the maximum boundary layer response in terms of disturbance energy for some given parameters (ξ_0, β, ω). The term 'global optimization' here refers to the optimal disturbance yielding the overall maximum energy gain at a given position x_1. Hence, to find a global optimal disturbance, we need to determine not only the optimal initial disturbance shape but also the optimal parameters (ξ_0, β, ω). We obtain these by employing a quasi-Newton line search optimization based on a finite-difference Jacobian as in Tempelmann *et al.* (2010*b*). Global optimal disturbances are thus computed by combining the adjoint-based optimization yielding the optimal disturbance shape with a quasi-Newton approach providing the optimal parameters (ξ_0, β, ω).

3. Baseflow

We want to study optimal growth in three-dimensional, compressible boundary layers including effects of curvature. We content ourselves with the study of three-dimensional boundary layers which are homogeneous in the spanwise direction. The model problem considered is a compressible boundary layer forming on both flat and curved swept plates that will reduce to a Falkner–Skan–Cooke boundary layer in the limiting case of zero Mach number and infinite radius of curvature. A sketch of a plate together with the used coordinate systems is shown in figure 1. In order to solve the quasi-three-dimensional boundary layer equations we need to prescribe the tangential meanflow velocity component $\bar{U}_e$ at the boundary layer edge. The subscript 'e' denotes the boundary layer edge. We choose $\bar{U}_e$ and all related parameters such that the FSC boundary layer studied by Schrader, Brandt & Henningson (2009) is yielded in the previously mentioned limiting case. The pressure gradient considered by Schrader *et al.* (2009) was chosen to resemble that of a swept-wing boundary layer, which was studied experimentally by Saric and coworkers (see Reibert *et al.* 1996). Accordingly, we define

$$\frac{\bar{U}_e^d(\xi)}{\bar{U}_e^d(\xi_n)} = \left(\frac{\xi^d}{\xi_n^d}\right)^m, \tag{3.1}$$

$$\frac{\bar{V}_e^d}{\bar{U}_e^d(\xi_n)} = \tan(\Lambda), \tag{3.2}$$

where the superscript d denotes dimensional variables, $\xi_n^d = 167$ and $m = 0.2$. The sweep angle is $\Lambda = 45°$. The Reynolds number is $Re = \bar{U}_e^d(\xi_n) L_{ref}/\nu = 311.127$, where the reference length is chosen as $L_{ref} = 1$ and ν is the kinematic viscosity. The Mach number is defined as $Ma = \bar{U}_e^d(\xi_n)/\gamma R \bar{T}_e^d(\xi_n)$. The gas constant is chosen as $R = 287$, the specific heat ratio is $\gamma = 1.4$, the Prandtl number is assumed constant, $Pr = 0.72$, and $\bar{T}_e$ is obtained through isentropic relations where we choose the

https://doi.org/10.1017/jfm.2012.235 Published online by Cambridge University Press

stagnation temperature $\bar{T}_s^d = 300$ K. In order to integrate the boundary layer equations an initial profile is required. In the incompressible case we could have obtained such a profile from the Falkner–Skan–Cooke similarity solution presented by Cooke (1950). However, no similarity solution exists for the three-dimensional compressible boundary layer over a plate. Here, to obtain an initial profile, we assume local similarity (see e.g. Anderson 2006; Zuccher *et al.* 2006; Gaponov & Smorodskii 2008) and apply the 'Lees–Dorodnitsyn' transformation

$$\hat{x} = \int_0^{\xi} \bar{\rho}_e \bar{U}_e \mu_e \, \mathrm{d}\xi', \quad \hat{y} = \frac{\bar{U}_e}{\sqrt{2\hat{x}}} \int_0^{\eta} \bar{\rho} \, \mathrm{d}\eta', \tag{3.3}$$

to the three-dimensional, compressible boundary layer equations. Further, we introduce the similarity variables f, g, and Θ defined by

$$\bar{U} = \bar{U}_e f', \quad \bar{V} = \bar{V}_e g, \quad \bar{h} = \bar{T} c_p = \bar{h}_e \Theta. \tag{3.4}$$

The enthalpy is represented by $\bar{h}$, and c_p denotes the specific heat capacity. After neglecting all non-similar terms we obtain the ξ-momentum, ζ-momentum and energy equation as

$$(Cf'')' + ff'' - \frac{2\hat{x}}{\bar{U}_e}\left[(f')^2 - \frac{\rho_e}{\rho}\right]\frac{\mathrm{d}\bar{U}_e}{\mathrm{d}\hat{x}} = 0, \tag{3.5a}$$

$$(Cg')' + g'f = 0, \tag{3.5b}$$

$$\left(\frac{C}{Pr}\Theta'\right)' + f\Theta' + C\frac{\bar{U}_e^2}{\bar{h}_e}(f'')^2 + C\frac{\bar{V}_e^2}{\bar{h}_e}(g')^2 = 0, \tag{3.5c}$$

with $C = \bar{\rho}\mu/\bar{\rho}_e\mu_e$ and μ being the dynamic viscosity. These can be solved for any $\xi > 0$. Starting from that local approximate similarity solution, we can compute the boundary layer over the entire plate by simply integrating the full non-similar boundary layer equations in the downstream direction.

Throughout this paper we study the effect of different Mach numbers, wall cooling and curvature on optimal growth in three-dimensional boundary layers and therefore consider the following cases.

(i) Swept-flat-plate boundary layers with Mach numbers $Ma = 0.001, 0.75, 1.5$ and adiabatic walls, i.e. $\bar{T}_w/\bar{T}_{ad} = 1$. $\bar{T}_w$ represents some chosen wall temperature and $\bar{T}_{ad}$ denotes adiabatic wall temperatures implying the boundary condition $\partial\bar{T}/\partial\eta = 0$.

(ii) Swept-flat-plate boundary layers with Mach number $Ma = 0.75$ and two different wall temperatures, $\bar{T}_w/\bar{T}_{ad} = 0.5$ and $\bar{T}_w/\bar{T}_{ad} = 0.25$.

(iii) Boundary layers on swept plates with both concave and convex curvature, $Ma = 0.75$ and $\bar{T}_w/\bar{T}_{ad} = 1$. The radii are chosen as $R = 800$ and $R = 400$. Since for both radii the curvature parameter $\chi = \delta^*/R$ is of order $O(10^{-2})$, we do not consider any curvature terms when solving for the boundary layer flow. However, even slight curvature has a large effect on boundary layer stability. Curvature terms thus have to be included in the stability equation (2.2).

All these boundary layers were initiated with the approximate similarity solution at $\xi = 10$. Both external Mach number distributions and displacement thicknesses of the above boundary layers are shown in figure 2.

https://doi.org/10.1017/jfm.2012.235 Published online by Cambridge University Press

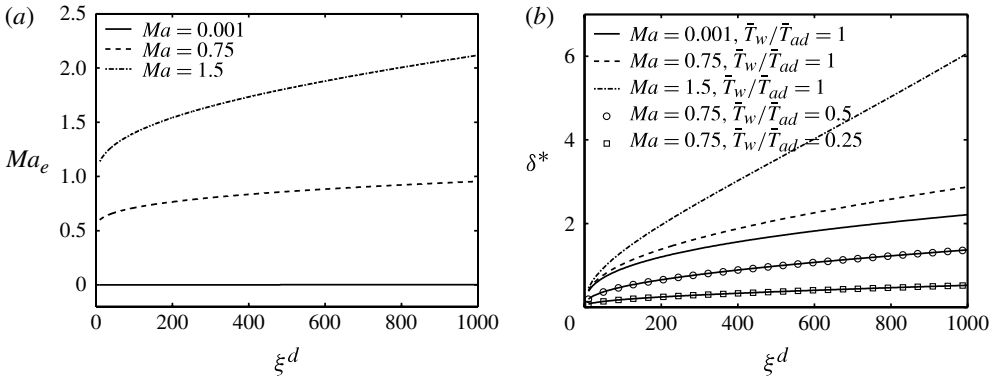


FIGURE 2. (*a*) Local Mach numbers Ma_e at the boundary layer edge for three different swept-plate boundary layers with $Ma = 0.001, 0.75, 1.5$. (*b*) Displacement thickness δ^* on the basis of $\bar{Q}$, which is the mean velocity component in the direction of the outer streamline, for swept-plate boundary layers with Mach numbers $Ma = 0.001, 0.75, 1.5$ and wall temperatures $\bar{T}_w/\bar{T}_{ad} = 0.25, 0.5, 1$.

4. Numerical approach & verification

The parabolized stability equation (2.2) is solved in MATLAB. The equation system is discretized using Chebyshev polynomials in the wall-normal direction. We use the 'MATLAB differentiation matrix suite' by Weideman & Reddy (2000). The Gauss–Lobatto collocation points are mapped to the domain $[0, \eta_{max}]$ and clustered near the wall using the mapping described in Hanifi *et al.* (1996). A second-order backward finite-difference scheme is employed to discretize the tangential direction ξ. The adjoint PSEs are discretized accordingly.

The ordinary differential equations (3.5) are solved using MATLAB's ODE solver in combination with a shooting method. The solution is used to initialize the full non-similar boundary layer equations which are solved by employing second-order finite differences in both the ξ- and η-directions.

The 'active-set' algorithm provided by MATLAB's optimization toolbox represents a quasi-Newton line-search method and is chosen for computing those parameters (ξ_0, β, ω) yielding global optimal disturbances as described in § 2.3.

To verify both the methodology described in § 2.1 and the related PSE code we compare the energy growth of an optimal disturbance predicted by the PSE approach to a corresponding direct numerical simulation (DNS). An optimal disturbance with $(\beta = 0.19, \omega = 0, \xi_0 = 167, \xi_1 = 1050)$ is computed for the incompressible FSC boundary layer using the methodology presented in § 2. The initial disturbance at ξ_0 is extracted from the PSE solution and prescribed as an inflow Dirichlet boundary condition for the DNS. Hence, at the inflow boundary of the DNS domain the disturbance is added to the FSC solution with a small amplitude to ensure linear growth. At the upper boundary of the DNS domain Dirichlet boundary conditions according to (3.1) are prescribed. The DNS was performed using the spectral element code 'Nek5000' by Fischer, Lottes & Kerkemeier (2008). Tempelmann *et al.* (2010*b*) have already compared the presented PSE method to a DNS of crossflow modes by Schrader *et al.* (2009) and obtained very good agreement. However, it is important to note that even in the initial region of strong non-modal growth both the PSE and the DNS results agree perfectly, as is evident in figure 3(*a*). Downstream of $\xi = 400$ the

https://doi.org/10.1017/jfm.2012.235 Published online by Cambridge University Press

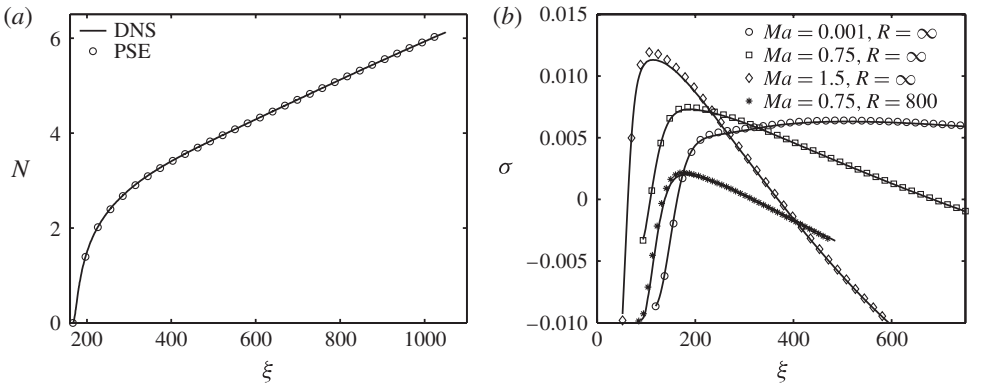


FIGURE 3. Comparison of the spatial evolution of an optimal perturbation with ($\beta = 0.19, \omega = 0$) in an incompressible swept-flat-plate boundary layer computed using the presented PSE method and a DNS. The DNS was performed with 'Nek5000' (see Fischer *et al.* 2008). (*b*) Growth rates of crossflow modes in different swept-plate boundary layers predicted by both the current method and the NOLOT code (see Hanifi *et al.* 1994). The growth rate is defined as $\sigma = \partial N/\partial\xi$. For a definition of N see (5.1). The different crossflow modes are: ($Ma = 0.001, R = \infty$) $\rightarrow$ ($\beta = 0.076, \omega = 0.0071$); ($Ma = 075, R = \infty$) $\rightarrow$ ($\beta = 0.14, \omega = 0.0095$); ($Ma = 1.5, R = \infty$) $\rightarrow$ ($\beta = 0.159, \omega = 0.019$); ($Ma = 0.75, R = 800$ (convex)) $\rightarrow$ ($\beta = 0.141, \omega = 0.0095$).

optimal disturbance turns into a crossflow mode whose growth is predicted identically by both methods. This successful comparison verifies the assumptions in § 2.1.

Further verification of the current PSE approach is given by comparing the predicted evolution of crossflow modes in different boundary layers to the one obtained from the NOLOT code developed by Hanifi *et al.* (1994). The latter code has been validated for a large number of different applications and represents an implementation of the classical PSE. Figure 3(*b*) shows the growth rate of crossflow modes in swept-plate boundary layers, both flat and curved, for different Mach numbers. Here too the agreement is very good. The slight differences are because of different choices of the wavenumber α. Here, we choose a real-valued wavenumber (see § 2.1) whereas α is chosen as a complex number in the NOLOT code. The latter choice ensures that the disturbance growth is mainly captured by the exponential part of the disturbance ansatz (2.1). This means that the disturbance pressure gradient represented by the term $\mathrm{i}\alpha p$ in the ξ-momentum equation not only accounts for the periodic variation of p' but also for its growth. Since we choose a real-valued wavenumber α only periodic variations of p' are represented by $\mathrm{i}\alpha p$. This explains the slight differences in figure 3(*b*). However, the overall good agreement confirms the assumption that the chordwise disturbance pressure gradient has a very small effect on the disturbance evolution.

We further verified the optimization approach by comparing to results of Andersson *et al.* (1999), Levin & Henningson (2003) and Tempelmann *et al.* (2010*b*) and obtained perfect agreement.

5. Results

In this section we study the effects that compressibility, wall cooling and curvature have on optimal growth and the corresponding disturbance shape in swept-plate

https://doi.org/10.1017/jfm.2012.235 Published online by Cambridge University Press

Ma	$\bar{T}_w/\bar{T}_{ad}$	R	ξ_{ne}	β	ω
0.001	1.0	∞	135	0.13–0.14	0.0079–0.0093
0.75	1.0	∞	101	0.14–0.16	0.0086–0.0167
1.5	1.0	∞	54	0.19–0.2	0.022–0.024
0.75	0.5	∞	456	0.05	5.5×10^{-4}–6.1×10^{-4}
0.75	0.25	∞	—	—	—
0.75	1.0	800 (concave)	59	0.14–0.17	-0.01–-0.0086
0.75	1.0	800 (convex)	225	0.1	0.015–0.016
0.75	1.0	400 (convex)	—	—	—

TABLE 1. Crossflow modes becoming first unstable in different swept-plate boundary layers as predicted by local stability theory. The position where they become unstable, i.e. the first neutral point of the respective boundary layer is denoted by ξ_{ne}. A dash is used if no unstable crossflow disturbances are found. The analysis is performed for $\xi \in [10, 1050]$.

boundary layers. Further, we investigate how the energy is distributed among the different disturbance variables. In the following all variables are presented in non-dimensional form. The reference length used for all variables, except ξ which is non-dimensionalized with $L_{ref} = 1$, is the displacement thickness δ^* at $\xi = 10$. The latter is computed on the basis of the meanflow velocity $\bar{Q}$, which is the velocity component in the direction of the outer streamline. Q_e, the respective meanflow velocity component at the boundary layer edge at $\xi = 10$, is chosen as the reference velocity. The disturbance energy growth is presented as N-factors of the form

$$N(\xi) = 0.5 \log\left(\frac{E(\xi)}{E(\xi_0)}\right). \tag{5.1}$$

The growth rate is then defined as $\sigma = \partial N/\partial \xi$.

5.1. *Local stability analysis*

Although we want to study spatial optimal growth in non-parallel boundary layers it makes sense to first perform a local stability analysis. Such a modal stability analysis will identify the first neutral points of crossflow modes, i.e. the position at which the first crossflow mode becomes unstable. As locally parallel flow is assumed, these positions are only approximate. However, in the non-parallel spatial framework the neutral point is not well defined as outlined by Tempelmann *et al.* (2010*b*). The neutral point of a crossflow mode computed using the PSE depends on where the disturbance was initiated.

Since we only want to get an idea of where the disturbance field is dominated by non-modal or modal disturbances, we content ourselves with a first neutral position on the basis of local stability theory. Upstream of that neutral point we assume the optimal disturbances to be of non-modal nature. Downstream, we expect to observe unstable crossflow disturbances of modal nature. Table 1 shows the result of the local stability analysis. One can see that, as long as the wall is not cooled, the first neutral position is moved upstream for increasing Mach numbers. Cooling the wall has quite a strong effect on the modal stability of crossflow disturbances. It is apparent from table 1 that cooling the wall to half the adiabatic temperature moves the first neutral point downstream to $\xi_{ne} = 456$ from $\xi_{ne} = 101$ in the adiabatic case. If the wall is cooled to a quarter of the adiabatic temperature no unstable crossflow modes are found

https://doi.org/10.1017/jfm.2012.235 Published online by Cambridge University Press

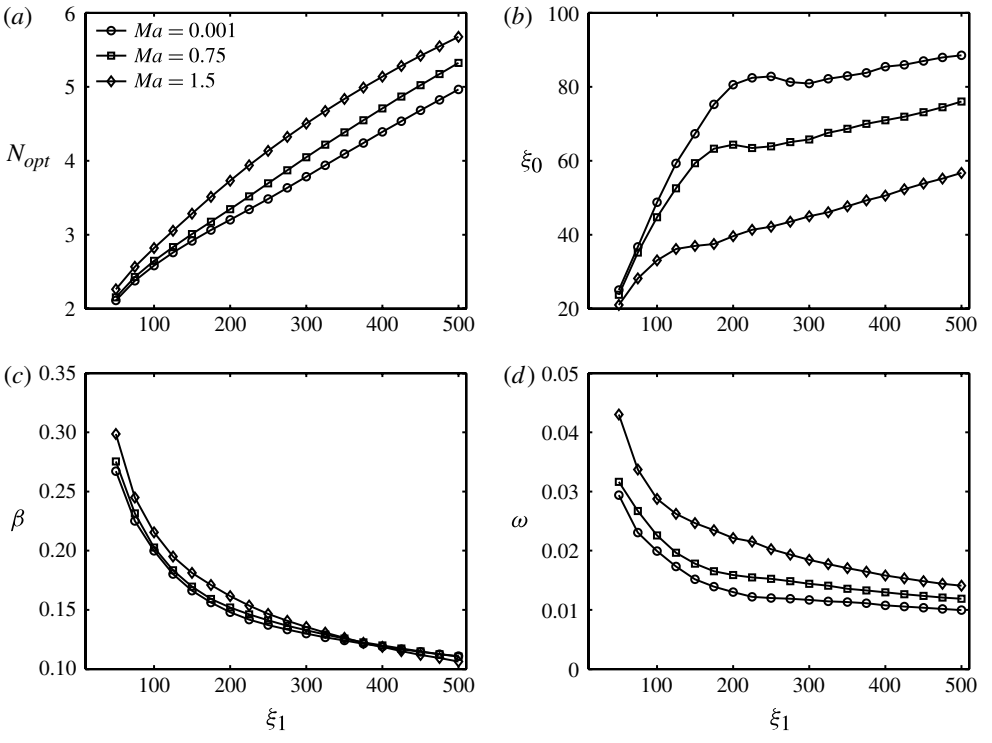


FIGURE 4. Mach number effects on optimal growth for boundary layers with $\bar{T}_w/\bar{T}_{ad} = 1$ and $R = \infty$. (*a*) N-factor of optimal growth for different ξ_1. (*b*) Optimal initial position ξ_0 versus ξ_1. (*c*) Optimal spanwise wavenumber β versus ξ_1. (*d*) Optimal radial frequency ω versus ξ_1.

in the considered domain. Convex curvature has a similar effect, but not as strong. Considering a radius of $R = 800$ moves the first neutral point to $\xi_{ne} = 225$. Concave curvature has a contrary effect, however, in that it strongly destabilizes the boundary layer. In the following we study optimal growth for boundary layers with $\xi \in [10, 500]$. This domain allows us to study optimal disturbances of both non-modal and modal nature for all chosen cases.

5.2. *Mach number effects*

To study the effects of compressibility, swept-flat-plate boundary layers with three different Mach numbers are considered. We compute global optimal disturbances for boundary layers with $Ma = 0.001$, $Ma = 0.75$ and $Ma = 1.5$. N-factors of global optimal growth as well as the optimal parameters (ξ_0, β, ω) are shown in figure 4. It can be seen from figure 4(*a*) that global optimal growth is increasing for higher Mach numbers. This trend is clear for all positions ξ_1. Figure 5 depicts $N(\xi)$ for all optimal disturbances presented in figure 4. Note that we obtain strong initial growth for all boundary layers and all ξ_1, even in those regions identified as subcritical with respect to modal growth in § 5.1. Indeed, for optimal disturbances with $\xi_1 < \xi_{ne}$ we observe extensive initial growth until the position of maximum amplification followed by rather quick decay. Disturbances whose energy growth has been maximized for $\xi_1 > \xi_{ne}$ also experience strong initial growth of non-modal nature. However, as depicted in figure 6, downstream of this initial region of non-modal growth, optimal disturbances become

https://doi.org/10.1017/jfm.2012.235 Published online by Cambridge University Press

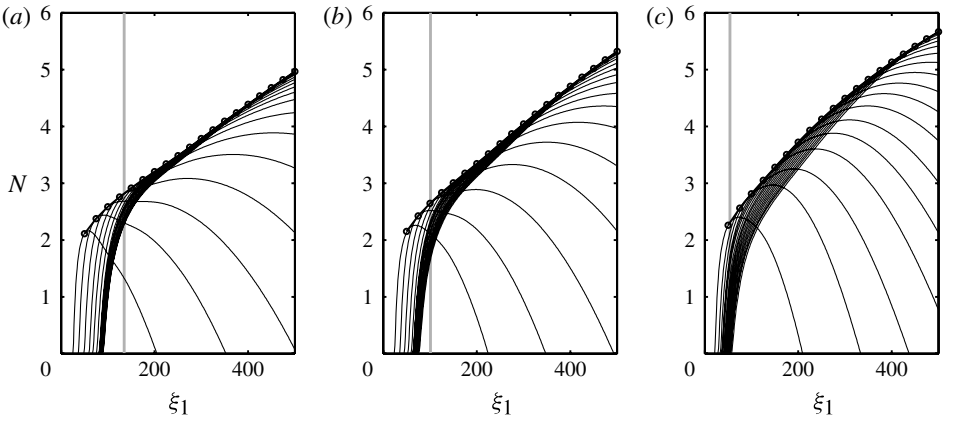


FIGURE 5. N-factors $N(\xi)$ of optimal disturbances obtained for different Mach numbers. Each disturbance has been optimized to experience maximum energy growth at the position ξ_1 marked by the circles. The grey line denotes the position of the first neutral point as predicted by local theory (see table 1). (*a*) $Ma = 0.001$, (*b*) $Ma = 0.75$, (*c*) $Ma = 1.5$.

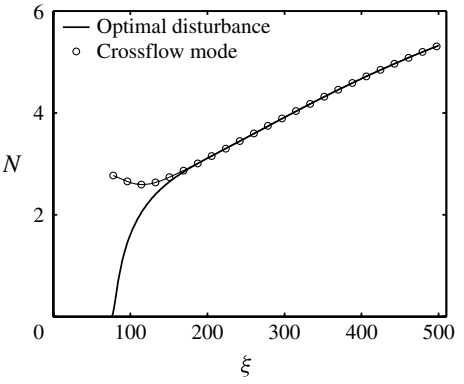


FIGURE 6. N-factors of a global optimal disturbance obtained for $\xi_1 = 500$, $R = \infty$, $\bar{T}_w/\bar{T}_{ad} = 1$, $Ma = 0.75$ and the corresponding crossflow mode. The latter is initialized with a solution to the local stability equations.

of modal nature and turn into crossflow modes. These observations conform to earlier results by Corbett & Bottaro (2001) and Tempelmann *et al.* (2010*b*) for incompressible flow. It becomes clear from figure 5 that the initial non-modal growth of global optimal disturbances attains N-factors between 2 and 3 for all boundary layers and any ξ_1 studied here. Also, these values correspond to results by Tempelmann *et al.* (2010*b*) for incompressible FSC boundary layers.

Figure 4(*b*) shows that the optimal initial position ξ_0 moves downstream for increasing ξ_1. Initially, the increase of the optimal ξ_0 is quite rapid. This rapid increase is because of the subcritical nature of the boundary layer flow upstream of the first neutral point. Non-modal disturbances only grow over short distances in this region and decay rapidly further downstream. Hence, in order to attain maximum energy growth an optimal disturbance has to be initiated close to the position of maximum

https://doi.org/10.1017/jfm.2012.235 Published online by Cambridge University Press

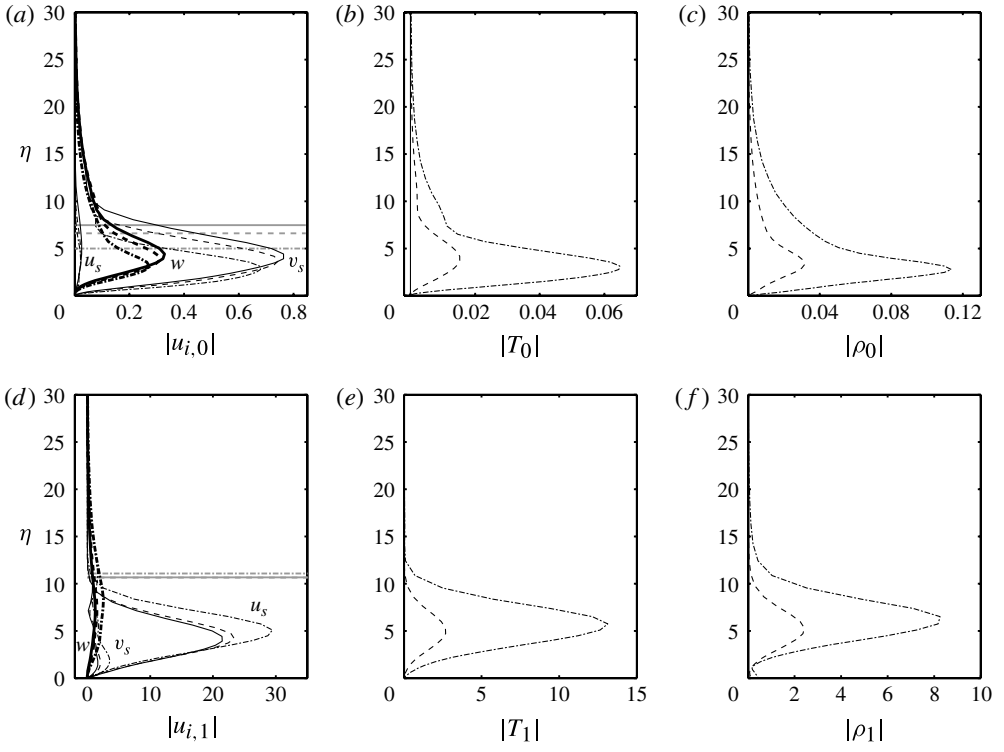


FIGURE 7. Absolute values of (u_s, v_s, w, T, ρ) of optimal disturbances at (*a–c*) ξ_0 and (*d–f*) ξ_1. The position of maximum amplification is $\xi_1 = 200$ for all boundary layers: —, $Ma = 0.001$; - - -, $Ma = 0.75$; ···, $Ma = 1.5$. The w-component is plotted with thick lines. The respective boundary layer thicknesses $\delta_{99.5}$ are depicted by the horizontal grey lines.

amplification. Downstream of the first neutral point crossflow modes become optimal disturbances. Since these grow over long streamwise distances, maximum disturbance growth is obtained for initial positions just upstream of the neutral point of the corresponding crossflow mode (see figure 6). The transition between these two regimes is characterized by a slight overshoot apparent in figure 4(*b*). This overshoot is less distinct for $Ma = 1.5$ because the neutral point is located far upstream yielding a boundary layer which is almost entirely dominated by modal growth. The fact that the boundary layers become more unstable to modal disturbances for higher Mach numbers (see § 5.1) thus explains why the optimal ξ_0 decreases when Ma is increased.

The optimal spanwise wavenumbers depicted in figure 4(*c*) are similar for all three boundary layers and decrease for increasing ξ_1. The non-dimensional radial frequency also decreases for increasing ξ_1, but it takes larger values for higher Mach numbers.

Further, we want to investigate if compressibility has any effect on the shape of optimal disturbances and the physical mechanisms of optimal growth. Therefore, we plot the absolute values of (u_s, v_s, w, T, ρ) at ξ_0 and ξ_1 for all three boundary layers in figure 7. We choose those optimal disturbances whose energy growth is maximized for $\xi_1 = 200$. The subscript 's' denotes velocity components in a coordinate system which is aligned with the line of constant phase of the optimal disturbances. The orientation of such a coordinate system is different for each position ξ. Hence, u_s is in the direction of the line of constant phase. It is apparent that the disturbance shapes

https://doi.org/10.1017/jfm.2012.235 Published online by Cambridge University Press

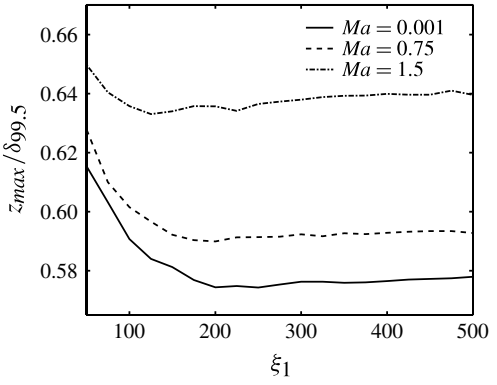


FIGURE 8. Location of the peak of w of the initial optimal disturbance with respect to the boundary layer thickness $\delta_{99.5}$ at the respective optimal initial position ξ_0. The peak location z_{max} is plotted versus each corresponding position of maximum amplification ξ_1.

obtained for different Mach numbers are very similar. Both the v_s-component and the w-component dominate over the u_s-component at ξ_0. This agrees with the results by Tempelmann *et al.* (2010*b*) and indicates that the initial disturbance takes the form of streamwise vortices. By transforming the optimal disturbance of the boundary layer with $Ma = 0.75$ to physical space, this is confirmed (see figure 9). As in the case considered by Tempelmann *et al.* (2010*b*), the initial disturbance takes the form of streamwise vortices which are tilted against the direction of the mean crossflow shear. While evolving downstream they rise to an upright position and develop into streaky disturbances characterized by a dominant u_s-component. This is nicely depicted in figure 7(*d*).

The temperature as well as the density component of the optimal disturbances are shown in figure 7(*b,c*) and figure 7(*e,f*). They have a very similar shape at ξ_0 and at ξ_1. However, their amplitudes increase with increasing Mach number starting from almost zero for $Ma = 0.001$. Figure 10 reveals that both the temperature and the density components of the optimal disturbance take the form of streaks of alternating high and low temperature and density respectively. Note that the phase difference between disturbance temperature and density is π.

Figures 7(*a*) and 7(*d*) also depict the wall-normal locations of the respective boundary layer edges in form of the boundary layer thickness $\delta_{99.5}$, which is computed on the basis of the meanflow velocity component $\bar{Q}$. It is apparent that the optimal initial disturbances extend into the free stream but are mainly located inside the boundary layer. Receptivity to free-stream disturbances would thus be most efficient for disturbances penetrating deep into the boundary layer. However, plotting the position z_{max} of the peak values of $|w(\xi_0)|$ normalized with $\delta_{99.5}(\xi_0)$ versus ξ_1 (see figure 8) shows that the optimal initial disturbances move closer to the boundary layer edge for smaller ξ_1. We can thus expect the receptivity to free-stream disturbances to become more efficient the closer we get to the leading edge, which is not considered here. The optimal disturbances at the position of maximum amplification depicted in figure 7(*d*) are located almost entirely within the boundary layer.

Another possibility for investigating the effect of compressibility on optimal disturbances is to study how the energy is distributed among the different disturbance components. We therefore compute the contribution of each disturbance component

https://doi.org/10.1017/jfm.2012.235 Published online by Cambridge University Press

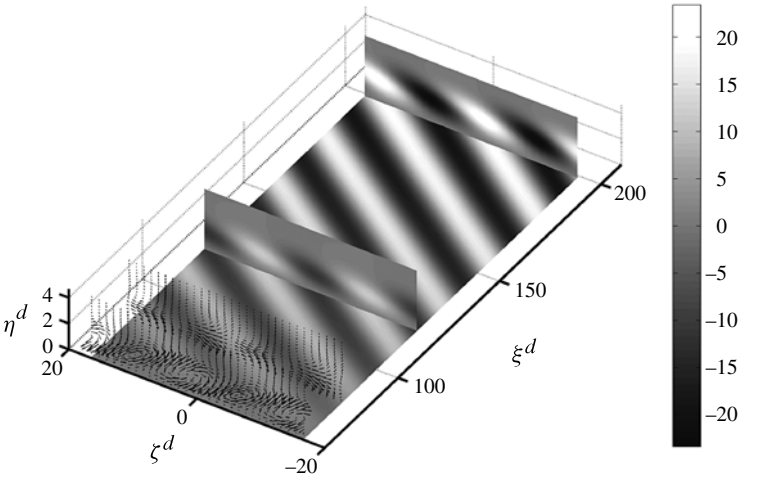


FIGURE 9. Three-dimensional visualization of optimal disturbance in physical space. $Ma = 0.75$, $\xi_1 = 200$. The pseudocolours represent the 'streak'-component u_s of the disturbance while arrows represent full velocity vectors. For visualization purposes the horizontal plane at $\eta^d = 1.3$ is shifted to $\eta^d = 0$.

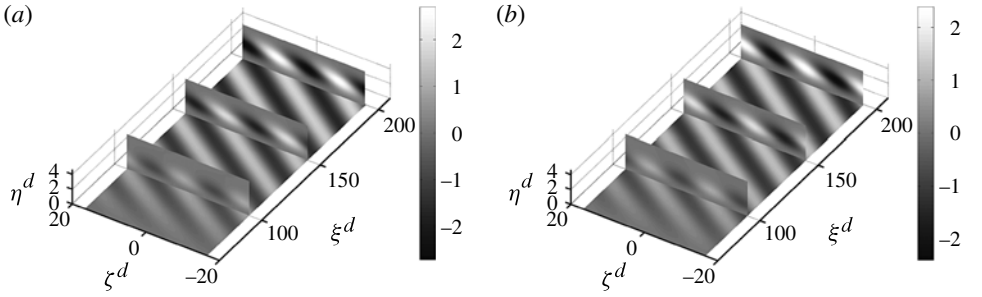


FIGURE 10. Three-dimensional visualization of optimal disturbance in physical space. $Ma = 0.75$, $\xi_1 = 200$. (*a*) Pseudocolours of the disturbance temperature. (*b*) Pseudocolours of the disturbance density.

to the energy norm (2.5) individually and normalize it with the total energy. Hence, a sum of all the normalized individual energies is identical to one. Figure 11 shows the individual energy norms for the optimal disturbances presented in figure 7. For $Ma = 0.001$ the energy distribution shown in figure 11(*a*) is as one might expect from figure 7 and previous studies. Initially the energy is mostly concentrated in the v- and w-components. Further downstream streaks dominate, and almost all energy is contained in u and v. For higher Mach numbers, however, the fraction of the energy contained in the temperature and density components increases. In the case of $Ma = 1.5$, 16 % of the energy at the position of maximum amplification is contained in the disturbance temperature while the density component contributes with 7 %.

On the basis of the latter results we find that the physical mechanisms for optimal growth in compressible boundary layers are similar to those identified for the incompressible case by Corbett & Bottaro (2001) and Tempelmann *et al.* (2010*b*).

https://doi.org/10.1017/jfm.2012.235 Published online by Cambridge University Press

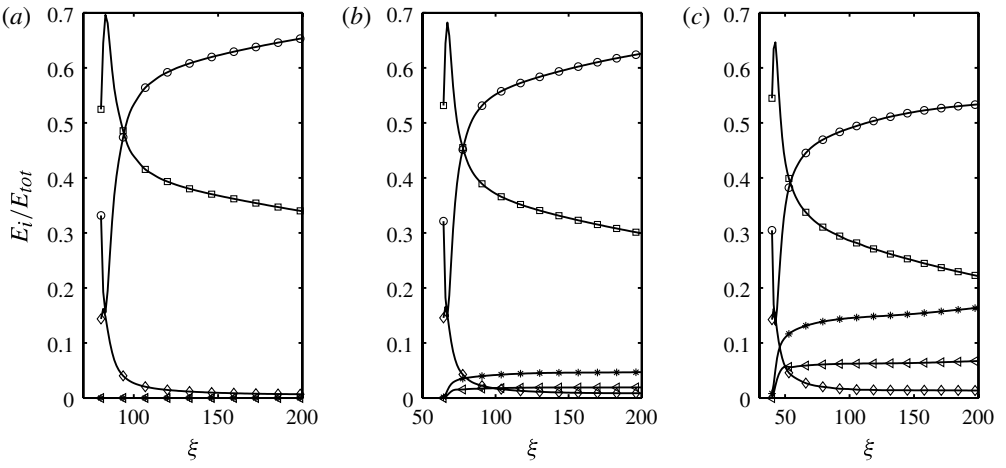


FIGURE 11. Distribution of energy among the different components of an optimal disturbance with $\xi_1 = 200$, $R = \infty$ and $\bar{T}_w/\bar{T}_{ad} = 1$: $\circ$, E_u/E_{tot}; $\square$, E_v/E_{tot}; $\diamond$, E_w/E_{tot}; $\star$, E_T/E_{tot}; $\triangleleft$, E_ρ/E_{tot}. (*a*) $Ma = 0.001$, (*b*) $Ma = 0.75$, (*c*) $Ma = 1.5$.

One mechanism is the well-known lift-up effect, where streamwise vortices produce streaky structures by displacing fluid particles vertically, which keep their horizontal momentum. The initially tilted vortices point to the existence of a second mechanism, as was pointed out by Tempelmann *et al.* (2010*b*). This mechanism is referred to as the Orr mechanism, where tilted vortices extract energy from the meanflow while being erected.

5.3. *Wall cooling*

In this section we investigate the effect of wall cooling on optimal growth. The boundary layer with a Mach number $Ma = 0.75$ and $\bar{T}_w/\bar{T}_{ad} = 1$ presented in the previous section is chosen as a reference. Additionally, we compute global optimal disturbances for boundary layers with $\bar{T}_w/\bar{T}_{ad} = 0.5$ and $\bar{T}_w/\bar{T}_{ad} = 0.25$. Figure 12 shows the optimization results for the three different boundary layers. It is very interesting that wall cooling destabilizes the boundary layer in regions which are dominated by non-modal growth (see figures 12*a* and 13). The growth of modal disturbances on the other hand, i.e. that of crossflow modes, is attenuated by wall cooling. From table 1 and figure 13(*c*) it is evident that no unstable modes exist in the domain of interest. Cooling the wall with $\bar{T}_w/\bar{T}_{ad} = 0.25$ stabilizes the boundary layer completely with respect to modal instabilities. However, upstream of $\xi_1 = 200$ it is this boundary layer which exhibits maximum optimal growth. Figure 13 shows that these disturbances are all of non-modal nature. They experience rapid initial growth up to the position of maximum amplification and decay downstream of it. As expected from the previous results, the optimal initial positions move downstream once the boundary layer becomes stable to modal disturbances. Hence, ξ_0 increases with increasing $\bar{T}_w/\bar{T}_{ad}$. Another interesting result of the optimization is that the optimal radial frequency ω is decreased strongly by wall cooling. For $\bar{T}_w/\bar{T}_{ad} = 0.25$ the non-dimensional frequency yielding global optimal growth is close to zero for all ξ_1 (see figure 12). The general trend observed in the previous sections, i.e. ω decreases for increasing ξ_1, is still apparent for $\bar{T}_w/\bar{T}_{ad} = 0.5$. The same trend can be observed

https://doi.org/10.1017/jfm.2012.235 Published online by Cambridge University Press

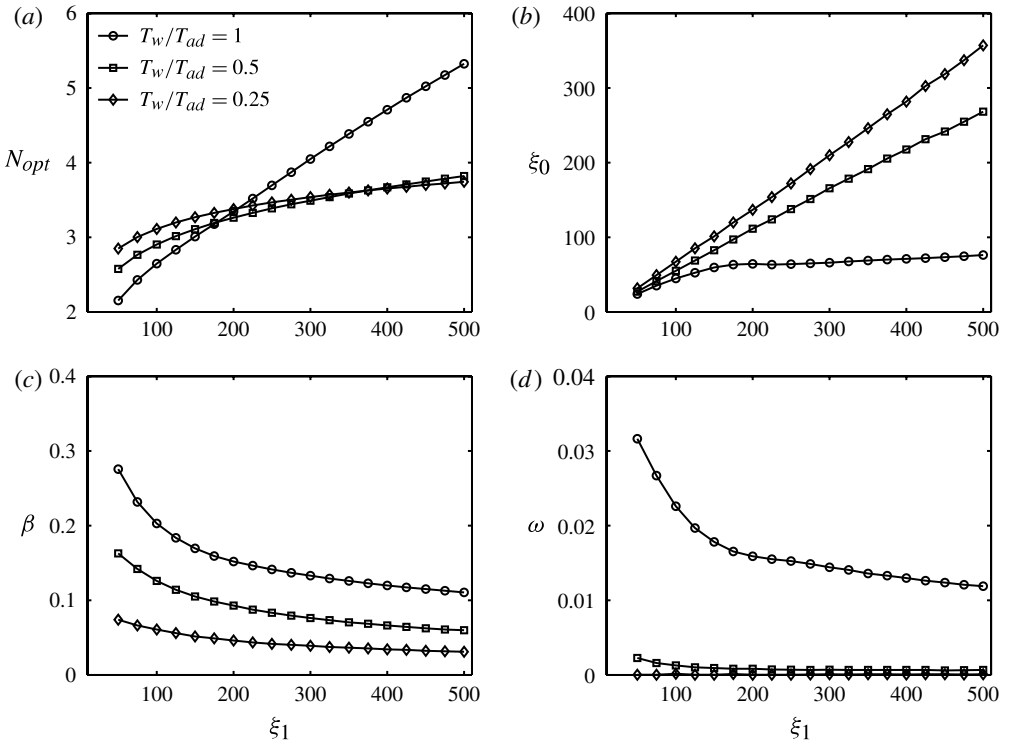


FIGURE 12. Effects of wall cooling on optimal growth for boundary layers with $Ma = 0.75$ and $R = \infty$. (*a*) N-factor of optimal growth for different ξ_1. (*b*) Optimal initial position ξ_0 versus ξ_1. (*c*) Optimal spanwise wavenumber β versus ξ_1. (*d*) Optimal radial frequency ω versus ξ_1.

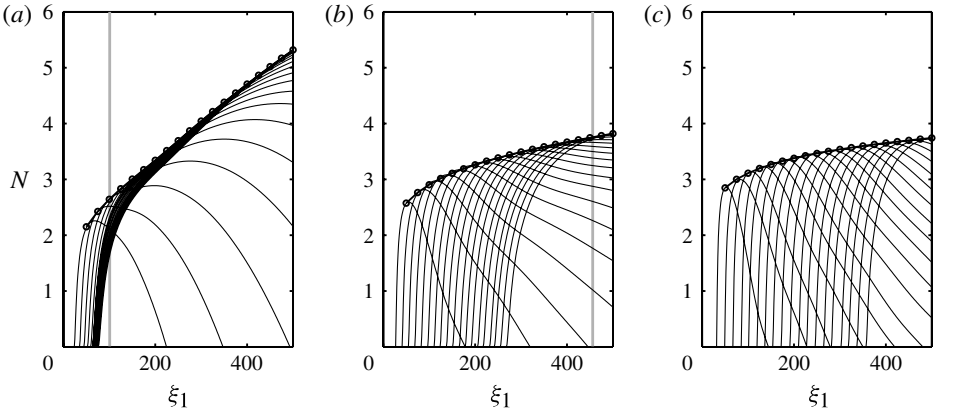


FIGURE 13. N-factors $N(\xi)$ of optimal disturbances for boundary layers with different wall temperatures. Each disturbance has been optimized to experience maximum energy growth at the position ξ_1 marked by the circles. The grey line denotes the position of the first neutral point as predicted by local theory (see table 1). (*a*) $\bar{T}_w/\bar{T}_{ad} = 1$, (*b*) $\bar{T}_w/\bar{T}_{ad} = 0.5$, (*c*) $\bar{T}_w/\bar{T}_{ad} = 0.25$.

https://doi.org/10.1017/jfm.2012.235 Published online by Cambridge University Press

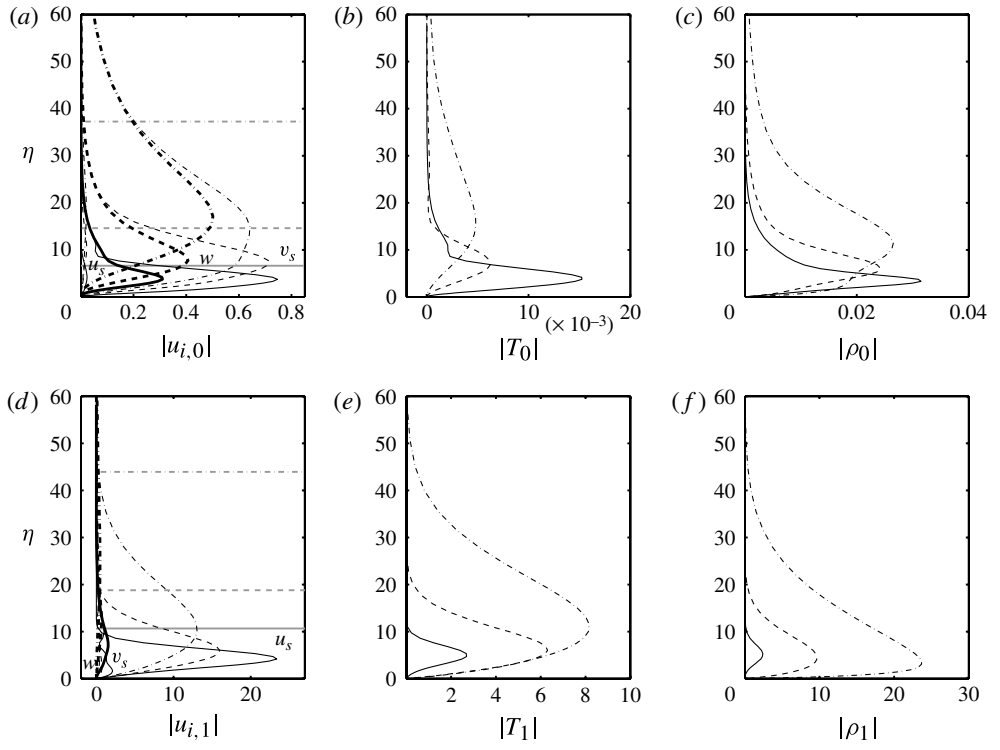


FIGURE 14. Absolute values of (u_s, v_s, w, T, ρ) of optimal disturbances at $(a–c)$ ξ_0 and $(d–f)$ ξ_1. The position of maximum amplification is $\xi_1 = 200$ for all boundary layers: —, $\bar{T}_w/\bar{T}_{ad} = 1$; - - -, $\bar{T}_w/\bar{T}_{ad} = 0.5$; ···, $\bar{T}_w/\bar{T}_{ad} = 0.25$. The Mach number is $Ma = 0.75$. The w-component is plotted with thick lines. The respective boundary layer thicknesses $\delta_{99.5}$ are depicted by the horizontal grey lines.

for the optimal spanwise wavenumbers in figure 12. Further, we find that lower wall temperatures lead to lower optimal spanwise wavenumbers.

Figure 14 presents the shape functions of the global optimal disturbance for $\xi_1 = 200$ at the initial and final positions. A close look reveals no principal differences between the optimal disturbances obtained for boundary layers with cooled walls and that with an adiabatic wall. Even if the peak-values are not located at similar wall-normal positions η we still observe that the velocity components w and v_s dominate over u_s initially. Downstream streaks develop and the corresponding velocity component u_s dominates. If we were to plot the velocities in physical space as figure 9, we would again find that the optimal disturbances take the form of tilted vortices initially and develop into streaks further downstream. Hence, wall cooling does not affect the physical mechanisms of disturbance growth in three-dimensional boundary layers. Further, temperature and density disturbances take the form of streaks as in the adiabatic cases. Figure 14(*b*) shows that the maximum amplitude of the optimal initial temperature disturbance decreases for lower wall temperatures. However, at the position of maximum amplification we observe the opposite trend, i.e. the maximum amplitude increases for lower wall temperatures. Similarly, the maximum density amplitude at ξ_1 increases when decreasing the wall temperature. At ξ_0, however, the

https://doi.org/10.1017/jfm.2012.235 Published online by Cambridge University Press

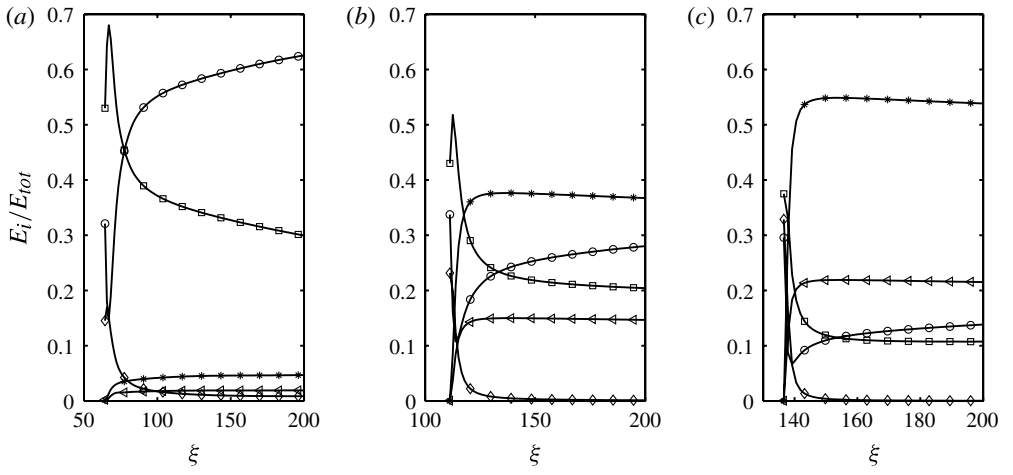


FIGURE 15. Distribution of energy among the different components of an optimal disturbance with $\xi_1 = 200$: $\circ$, E_u/E_{tot}; $\square$, E_v/E_{tot}; $\diamond$, E_w/E_{tot}; $\star$, E_T/E_{tot}; $\triangleleft$, E_ρ/E_{tot}. (*a*) $\bar{T}_w/\bar{T}_{ad} = 1$, (*b*) $\bar{T}_w/\bar{T}_{ad} = 0.5$, (*c*) $\bar{T}_w/\bar{T}_{ad} = 0.25$.

amplitudes are quite similar. As for the adiabatic cases we find that the optimal initial disturbances extend into the free stream. However, their peak values are well inside the boundary layer. At the position of maximum amplification they are located almost entirely inside the boundary layer.

Figure 15, where we plot the individual energy contributions, nicely depicts the emergence of streaks and the growth of temperature and density disturbances. It is evident that, compared to the reference adiabatic case shown in figure 15(*a*), the contributions of temperature and density disturbances to the energy norm (2.5) increase for cooled walls. Note that for $\bar{T}_w/\bar{T}_{ad} = 0.5$ the temperature component contributes with 37 % while for $\bar{T}_w/\bar{T}_{ad} = 0.25$ the contribution increases to even 54 %. The density contributions account for 15 and 22 % respectively. Hence, in the case of cooled walls, optimal disturbances are no longer dominated by disturbance velocities but by temperature and density components. The reason for this is found from the meanflow gradients for temperature and density inside the boundary layer. The more the wall is cooled the steeper these gradients become. Steeper gradients in turn lead to a more effective lift-up mechanism, which explains why temperature and density streaks become very strong when wall cooling is employed.

5.4. *Curvature effects*

Finally, we want to investigate what effect curvature has on optimal growth in a three-dimensional, compressible boundary layer. We study effects of both concave and convex curvature. Figure 16 shows the results of the global optimization for swept plates with different curvatures, $Ma = 0.75$ and $\bar{T}_w/\bar{T}_{ad} = 1$, and compares them to the reference flat plate case. It is apparent from figure 16 that effects of curvature are similar in both sub- and supercritical regions of the boundary layer. We find that concave curvature has a destabilizing effect on non-modal as well as modal disturbances, whereas convex curvature has a stabilizing effect. However, curvature affects the stability of crossflow modes much more strongly compared with the stability of non-modal disturbances. The growth curves diverge the further ξ_1 is located downstream. In the case of $R = 400$, which is completely stable to modal disturbances,

https://doi.org/10.1017/jfm.2012.235 Published online by Cambridge University Press

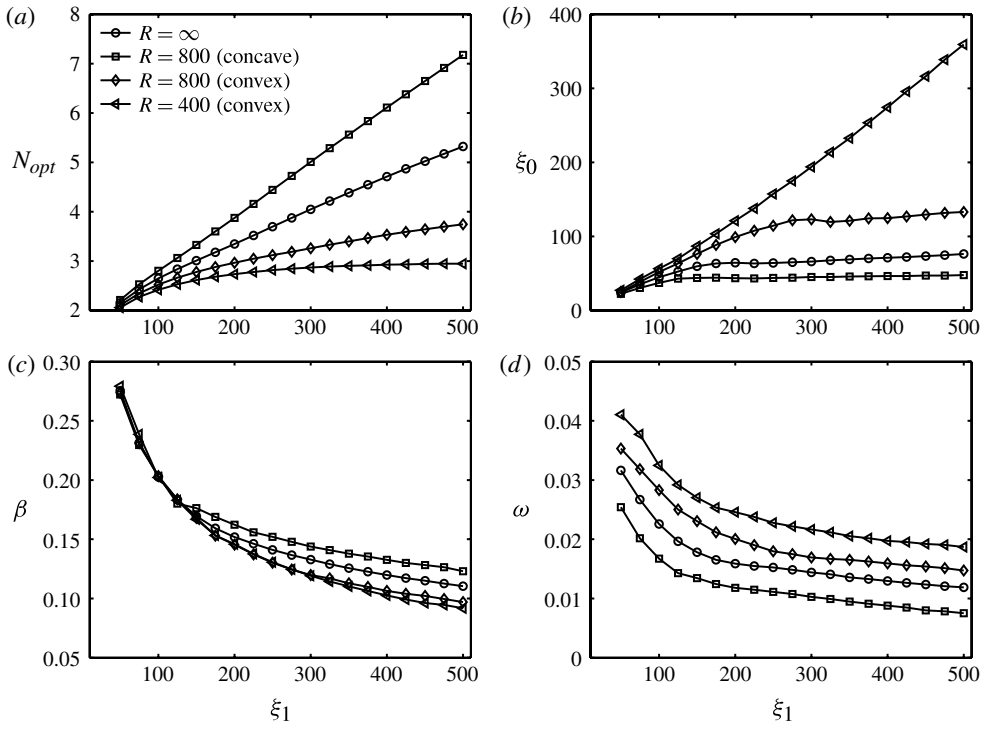


FIGURE 16. Effects of wall curvature on optimal growth for boundary layers with $Ma = 0.75$ and $\bar{T}_w/\bar{T}_{ad} = 1$. (*a*) N-factor of optimal growth for different ξ_1. (*b*) Optimal initial position ξ_0 versus ξ_1. (*c*) Optimal spanwise wavenumber β versus ξ_1. (d) Optimal radial frequency ω versus ξ_1.

maximum N-factors up to 3 are obtained. When considering concave curvature with $R = 800$, we obtain maximum N-factors up to 7. In the initial region, where non-modal growth is dominating the disturbance field of all four boundary layers, global optimal growth is of similar order, i.e. the corresponding N-factors are between 2 and 3.

The optimal initial position ξ_0 shown in figure 16 again follows the trend identified previously. Hence, the more stable the boundary layer, the closer ξ_0 is located upstream of ξ_1. This leads to optimal initial positions moving downstream when changing from concave curvature towards convex curvature. Figure 16(*c*) shows that the optimal spanwise wavenumber is similar in all boundary layers where non-modal disturbances dominate, i.e. for $\xi_1 < 100$ and for the cases with convex curvature. Where crossflow modes dominate, the optimal β increases when moving from convex to concave curvature. The optimal frequency follows a different trend compared to observations in §§ 5.2 and 5.3. Here, we observe that ω increases when moving from concave to convex curvature. This means that ω is smallest for the most unstable boundary layer, which is the opposite of our findings for boundary layers with cooled walls. Further, we investigate whether curvature has any effect on the optimal disturbance shape and the physical mechanisms of optimal growth in three-dimensional boundary layers. Therefore we compare the optimal disturbance shape of a case with concave curvature and one with convex curvature to the reference flat-plate boundary layer with Mach number $Ma = 0.75$ (see figure 17). It becomes apparent that the optimal disturbance shapes are very similar both at the initial position as well as at

https://doi.org/10.1017/jfm.2012.235 Published online by Cambridge University Press

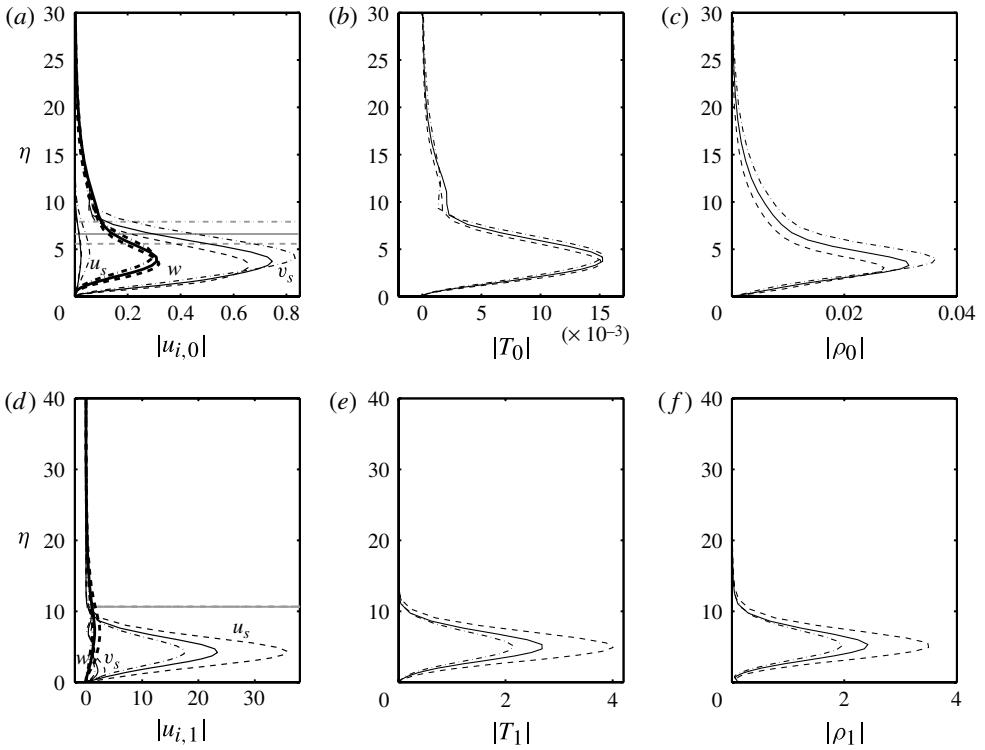


FIGURE 17. Absolute values of (u_s, v_s, w, T, ρ) of optimal disturbances at (*a–c*) ξ_0 and (*d–f*) ξ_1. The position of maximum amplification is $\xi_1 = 200$ for all boundary layers: —, $R = \infty$; - - -, $R = 800$ (concave); -·-, $R = 800$ (convex). The Mach number is $Ma = 0.75$. The w-component is plotted with thick lines. The respective boundary layer thicknesses $\delta_{99.5}$ are depicted by the horizontal grey lines.

the position of maximum amplification. Further, the energy evolution is very similar for all boundary layer cases considered as is shown in figure 18. This means that the same physical growth mechanisms as those described in §§ 5.2 and 5.3 appear to be at hand. These are the lift-up mechanism, which generates strong streaks of velocity, temperature and density disturbances, and the Orr mechanism.

6. Conclusions

An extension of the methodology developed by Tempelmann *et al.* (2010*b*) to compressible flow including curvature effects has been presented. Optimal growth has been studied for compressible boundary layers of swept flat plates with both cooled and adiabatic walls as well as for boundary layers on swept curved plates with both convex and concave curvature.

The methodology presented here is based on the parabolized stability equations and allows us to predict the spatial evolution of disturbances in compressible, three-dimensional boundary layers. The disturbances can be of modal as well as non-modal nature and curvature effects are accounted for. This methodology is therefore more general than the classical PSE approach, which is used only to predict the evolution of modal disturbances. A quasi-Newton line search method on the basis of finite-difference Jacobians has been used in combination with adjoint-based optimization to

https://doi.org/10.1017/jfm.2012.235 Published online by Cambridge University Press

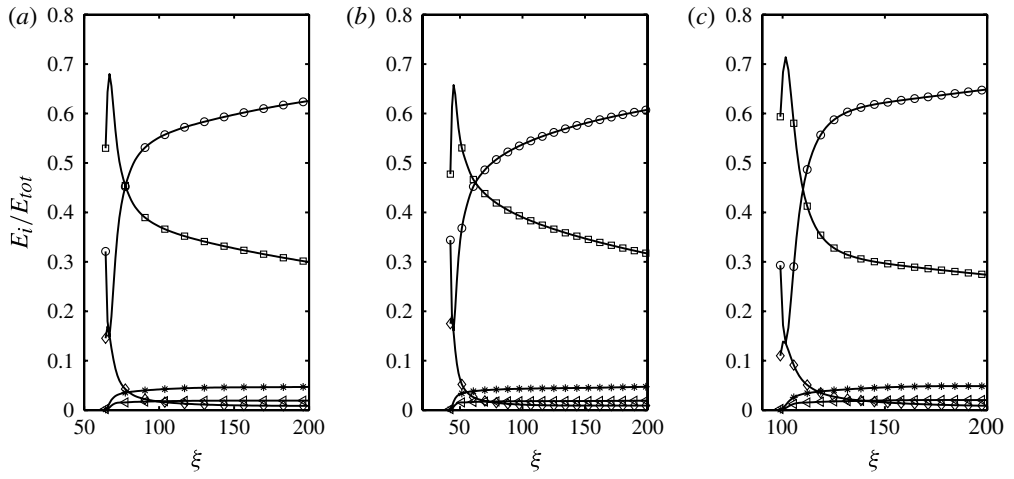


FIGURE 18. Distribution of energy among the different components of an optimal disturbance with $\xi_1 = 200$: $\circ$, E_u/E_{tot}; $\square$, E_v/E_{tot}; $\diamond$, E_w/E_{tot}; $\star$, E_T/E_{tot}; $\triangleleft$ E_ρ/E_{tot}. (*a*) $R = \infty$, (*b*) $R = 800$ (concave), (*c*) $R = 800$ (convex).

find those disturbances which experience maximum energy growth within a specified domain.

Extensive non-modal disturbance growth is found at all positions in all considered boundary layers, even in regions which are subcritical with respect to modal disturbances. When maximizing for regions which are supercritical, we observe that the boundary layer disturbances experience strong initial non-modal growth. Further downstream these disturbances become crossflow modes. In general we find that the physical mechanisms of optimal disturbance growth are identical for all studied boundary layer cases. They conform to the mechanisms identified for incompressible boundary layers by Corbett & Bottaro (2001) and Tempelmann *et al.* (2010*b*). These are the well-known lift-up effect, generating streamwise bent streaks, and the Orr mechanism, where tilted structures are erected by the mean crossflow shear. In addition to velocity streaks, the lift-up effect generates streaks of temperature and density disturbances in compressible boundary layers.

Global optimal growth has been computed for swept-flat-plate boundary layers at different Mach numbers. The maximum energy growth obtained at different positions on the plate increases for higher Mach numbers. The higher the Mach number the higher is the contribution of temperature and density to the energy norm (2.5). However, the contribution of the disturbance velocity component u_s has been dominant for all considered Mach numbers. Although they are mainly located inside the boundary layer, we found that optimal initial disturbances extend into the free stream. The closer to the leading edge optimal disturbances are determined, the closer the peak values of the respective optimal initial disturbances move towards the boundary layer edge. We therefore conclude that receptivity to free-stream disturbances is most effective for deeply penetrating disturbances and increases for positions of inception farther upstream.

When cooling the wall we find that crossflow modes are highly damped whereas disturbances of non-modal nature are destabilized. This leads to a situation where, for $\bar{T}_w/\bar{T}_{ad} = 0.25$, the boundary layer experiences stronger optimal energy growth

https://doi.org/10.1017/jfm.2012.235 Published online by Cambridge University Press

in the domain $\xi_1 < 200$ than the corresponding adiabatic case. It should be kept in mind that the former boundary layer is completely stable to modal disturbances whereas the latter is unstable to crossflow modes. Using wall cooling as a control mechanism to shift the transition from laminar to turbulent flow downstream can thus be counterproductive in three-dimensional boundary layers since initial non-modal growth might be increased. Hence, although modal growth is damped, the strong initial growth could lead to early transition and shift the transition location upstream. These findings are similar to results obtained for two-dimensional boundary layers (see Tumin & Reshotko 2001) where TS waves are damped and streaks are destabilized by wall cooling.

Finally, the effect of wall curvature on optimal disturbance growth has been investigated. We find that concave curvature enhances both non-modal and modal growth whereas convex curvature has a stabilizing effect. Although curvature acts similarly on both modal and non-modal disturbances the latter are less affected in terms of growth.

The results for compressible boundary layers presented throughout this paper suggest that non-modal disturbance growth should be accounted for when developing models for transition prediction. Future work will therefore employ the presented methodology to predict the receptivity to free-stream disturbances. Such an analysis yields modal amplitudes that can be used to initiate nonlinear PSE computations. It thus allows for moving from transition models based on linear growth only towards amplitude-based transition prediction.

Acknowledgements

The authors gratefully acknowledge computer time provided by SNIC (Swedish National Infrastructure for Computing) at the Center for Parallel Computers (PDC) at KTH, Stockholm.

Appendix A. Coefficient of second viscosity

In this article we employed Stokes' hypothesis to determine the second viscosity coefficient λ, i.e.

$$\lambda + \tfrac{2}{3}\mu = 0. \tag{A 1}$$

However, different assumptions for λ have been used in the literature. Mack (1986) used $\lambda/\mu = -0.4/3$ while Zurigat, Nayfeh & Masad (1990) used $\lambda/\mu = -0.2/3$. It had been shown before, however, that the growth of first-mode instabilities such as Tollmien–Schlichting waves and crossflow modes is insensitive to the choice of λ (see e.g. Kufner 1995). Figure 19 shows the sensitivity of the growth rates of different crossflow modes. It is clear that the growth of these is not influenced by different choices of the second viscosity coefficient. This justifies the use of Stokes' hypothesis.

Appendix B. Choice of norm

As outlined in § 2.2 the choice of a norm to measure the disturbance evolution is not obvious for compressible fluids. We chose Mack's energy norm for the current study which, however, is postulated in spatial framework as it was rigorously derived within the temporal framework only by Mack (1969) and Hanifi *et al.* (1996). For incompressible flows the natural choice would be to use the kinetic energy. In this section we want to study briefly how the presented results are affected if we choose

https://doi.org/10.1017/jfm.2012.235 Published online by Cambridge University Press

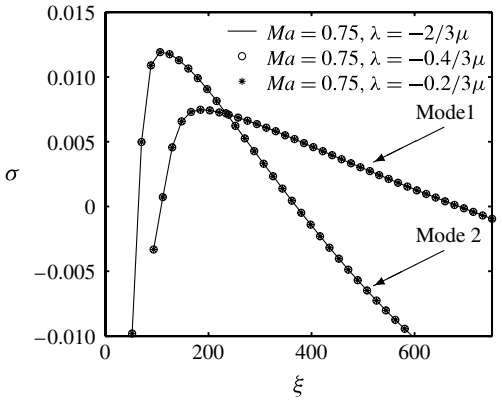


FIGURE 19. Sensitivity of the growth of two different crossflow modes with respect to the choice of the second viscosity coefficient λ. Mode 1: $(Ma = 075, R = \infty) \rightarrow (\beta = 0.14, \omega = 0.0095)$; Mode 2: $(Ma = 1.5, R = \infty) \rightarrow (\beta = 0.159, \omega = 0.019)$.

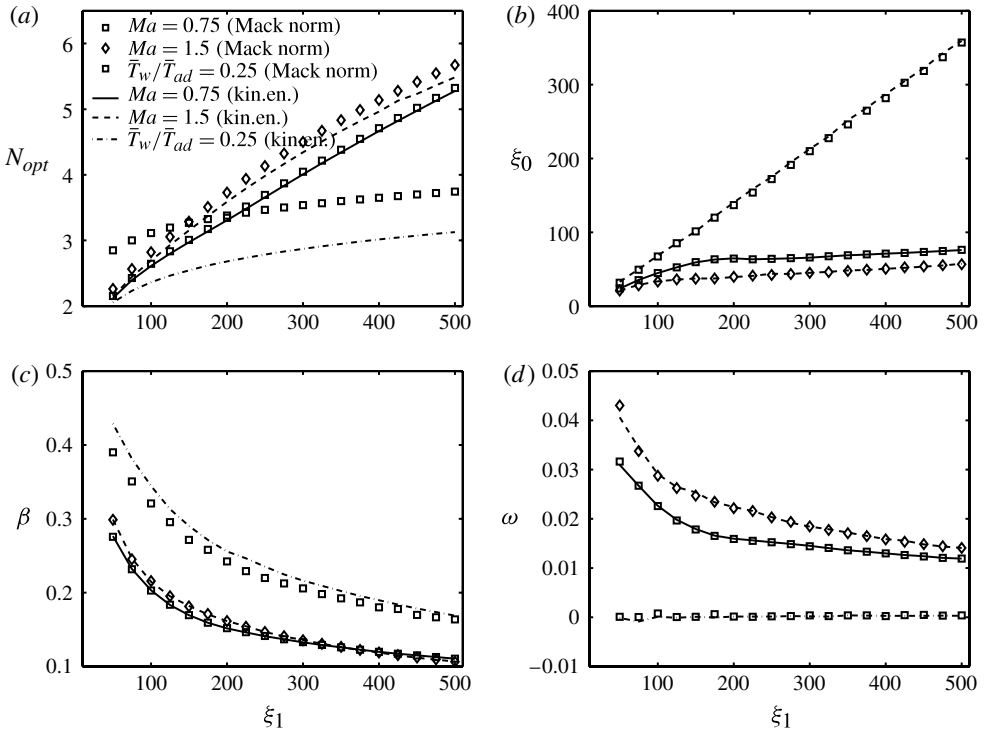


FIGURE 20. Effects on optimal growth if different norms are used for measuring disturbance growth. Either Mack's energy norm or the kinetic energy norm are used for cases with $(Ma = 0.75, \bar{T}_w/\bar{T}_{ad} = 1)$, $(Ma = 1.5, \bar{T}_w/\bar{T}_{ad} = 1)$, $(Ma = 0.75, \bar{T}_w/\bar{T}_{ad} = 0.25)$. (*a*) N-factor of optimal growth for different ξ_1. (*b*) Optimal initial position ξ_0 versus ξ_1. (*c*) Optimal spanwise wavenumber β versus ξ_1. (*d*) Optimal radial frequency ω versus ξ_1.

https://doi.org/10.1017/jfm.2012.235 Published online by Cambridge University Press

to measure disturbances using a norm based on kinetic energy. This will give us an impression of the sensitivity of the results with respect to the chosen norm.

Hence, in the following we replace Mack's energy norm (2.6) with the kinetic energy norm of the form

$$\boldsymbol{M}^{ke} = \mathrm{diag}[0, \bar{\rho}(\xi), \bar{\rho}(\xi), \bar{\rho}(\xi), 0]. \tag{B 1}$$

This choice leads to difficulties in determining the optimal initial condition $\boldsymbol{q}_0$ as $\boldsymbol{M}^{ke}$ becomes singular and cannot be inverted (see (2.12)). However, since we simply want to study the sensitivity of the results to the choice of norm, we follow the approach by Zuccher *et al.* (2006) and invert the submatrix of $\boldsymbol{M}^{ke}$ that determines (u_0, v_0, w_0) while we set $(\rho_0, T_0) = (0, 0)$. The results of an optimization using the kinetic energy norm for three different cases are shown in figure 20. For those cases involving an adiabatic wall the optimal parameters (ξ_0, β, ω) are above those obtained for Mack's energy norm. This means that either norm leads to the same optimal disturbances. The slight observable difference in optimal growth is because of the weak contribution of temperature and density to Mack's energy norm (see figure 11). Once the wall is cooled to 25 % of the adiabatic temperature, optimal parameters (ξ_0, β, ω) are still identical or close to those obtained with Mack's norm and yield similar optimal disturbances. However, the destabilization with respect to non-modal growth is no longer observed. This underlines the importance of using a norm that accounts for the contributions of disturbance temperature and density, as these become dominant for low wall temperatures (see figure 15).

REFERENCES

ANDERSON, J. D. 2006 *Hypersonic and High-Temperature Gas Dynamics*, 2nd edn. AIAA.

ANDERSSON, P., BERGGREN, M. B. & HENNINGSON, D. S. 1999 Optimal disturbances and bypass transition in boundary layers. *Phys. Fluids* **11**, 134–150.

ANDERSSON, P., HENNINGSON, D. S. & HANIFI, A. 1998 On a stabilization procedure for the parabolic stability equations. *J. Engng Math.* **33** (3), 311–332.

BERTOLOTTI, F. P. & HERBERT, T. 1991 Analysis of the linear stability of compressible boundary layers using the PSE. *Theor. Comput. Fluid Dyn.* **3**, 117–124.

BERTOLOTTI, F. P., HERBERT, T. & SPALART, P. R. 1992 Linear and nonlinear stability of the Blasius boundary layer. *J. Fluid Mech.* **242**, 441–474.

BIPPES, H. 1999 Basic experiments on transition in three-dimensional boundary layers dominated by cross-flow instability. *Prog. Aerosp. Sci.* **35**, 363–412.

BOTTARO, A. 2010 A receptive boundary layer. *J. Fluid Mech.* **646**, 1–4.

BREUER, K. S. & KURAISHI, T. 1994 Transient growth in two- and three-dimensional boundary layers. *Phys. Fluids* **6** (6), 1983–1993.

BUTLER, K. M. & FARRELL, B. F. 1992 Three-dimensional optimal perturbations in viscous shear flow. *Phys. Fluids* **4**, 1637–1650.

COOKE, J. C. 1950 The boundary layer of a class of infinite yawed cylinders. *Proc. Camb. Phil. Soc.* **46**, 645–648.

CORBETT, P. & BOTTARO, A. 2001 Optimal linear growth in swept boundary layers. *J. Fluid Mech.* **435**, 1–23.

COSSU, C., CHOMAZ, J.-M., HUERRE, P. & COSTA, M. 2000 Maximum spatial growth of Görtler vortices. *Flow Turbul. Combust.* **65**, 369–392.

ELLINGSEN, T. & PALM, E. 1975 Stability of linear flow. *Phys. Fluids* **18** (4), 487–488.

FISCHER, P. F., LOTTES, J. W. & KERKEMEIER, S. G. 2008 Nek5000 web page. http://nek5000.mcs.anl.gov.

FLÜGGE, S. & TRESDELL, C. 1959 *Handbuch der Physik, vol. VIII/1, Strömungsmechanik I.* Springer.

https://doi.org/10.1017/jfm.2012.235 Published online by Cambridge University Press

GAPONOV, S. A. & SMORODSKII, B. V. 2008 Linear stability of three-dimensional boundary layers. *J. Appl. Mech. Tech. Phys.* **49** (2), 157–166.

GRAVES, R. E. & ARROW, B. M. 1999 Bulk viscosity: past to present. *J. Thermodyn. Heat Transfer* **13** (3), 337–342.

HAJ-HARIRI, H. 1994 Characteristics analysis of the parabolized stability equations. *Stud. Appl. Math.* **92**, 41–53.

HANIFI, A. & HENNINGSON, D. S. 1998 The compressible inviscid algebraic instability for streamwise independent disturbances. *Phys. Fluids* **10** (8), 1784–1786.

HANIFI, A., HENNINGSON, D. S., HEIN, S., BERTOLOTTI, F. P & SIMEN, M. 1994 Linear non-local instability analysis: the linear NOLOT code. *FFA TN* **1994-54**.

HANIFI, A., SCHMID, P. J. & HENNINGSON, D. S. 1996 Transient growth in compressible boundary layer flow. *Phys. Fluids* **8** (3), 826–837.

KUFNER, E. 1995 Numerische Untersuchungen der Strömungsinstabilitäten an spitzen und stumpfen Kegeln bei hypersonischen Machzahlen. PhD thesis, DLR Göttingen.

KURIAN, T., FRANSSON, J. H. M. & ALFREDSSON, P. H. 2011 Boundary layer receptivity to free stream turbulence and surface roughness over a swept flat plate. *Phys. Fluids* **23**, 034107.

LANDAHL, M. T. 1980 A note on algebraic instability of inviscid parallel shear flows. *J. Fluid Mech.* **98**, 243–251.

LEVIN, O. & HENNINGSON, D. S. 2003 Exponential vs algebraic growth and transition prediction in boundary layer flow. *Flow Turbul. Combust.* **70**, 183–210.

LUCHINI, P. 2000 Reynolds-number-independent instability of the boundary layer over a flat surface: optimal perturbations. *J. Fluid Mech.* **404**, 289–309.

MACK, L. M. 1965 Computation of the stability of the laminar compressible boundary layer. *Meth. Comput. Phys.* **4**, 247.

MACK, L. M. 1969 Boundary layer stability theory. *JPL Rep.* 900-277. Jet Propulsion Laboratory, California Institute of Technology, Pasadena, CA, USA.

MACK, L. M. 1984 Boundary-layer linear stability theory. *AGARD Rep.* 709.

MACK, L. M. 1986 Boundary layer stability analysis for sharp cones at zero angle-of-attack. AFWAL-TR-86-3022, Flight Dynamics Laboratory, Air Force Wright Aeronautical Laboratories, Wright-Patterson AFB, Ohio, USA.

PRALITS, J. O., AIRIAU, C., HANIFI, A. & HENNINGSON, D. S. 2000 Sensitivity analysis using adjoint parabolized stability equations for compressible flows. *Flow Turbul. Combust.* **65**, 321–346.

REDDY, S. C. & HENNINGSON, D. S. 1993 Energy growth in viscous channel flow. *J. Fluid Mech.* **252**, 209–238.

REIBERT, M. S., SARIC, W. S., CARILLO, R. B. & CHAPMAN, K. L. 1996 Experiments in nonlinear saturation of stationary cross-flow vortices in a swept-wing boundary layer. *AIAA Paper* 96-0184.

RESHOTKO, E. & TUMIN, A. 2004*a* Optimal disturbances in the boundary layer over a sphere. *AIAA Paper* 2004-2241.

RESHOTKO, E. & TUMIN, A. 2004*b* Role of transient growth in roughness-induced transition. *AIAA J.* **42** (4), 766–770.

SCHRADER, L. U., BRANDT, L. & HENNINGSON, D. S. 2009 Receptivity mechanisms in three-dimensional boundary layer flows. *J. Fluid Mech.* **618**, 209–241.

SIMEN, M. 1992 Local and non-local stability theory of spatially varying flows. In *Instability, Transitions, and Turbulence*, pp. 181–195. Springer.

TEMPELMANN, D. 2009 Stability and receptivity of three-dimensional boundary layers. *TRITA-MEK* 2009:19, licentiate thesis, KTH Stockholm.

TEMPELMANN, D., HANIFI, A. & HENNINGSON, D. S. 2010*a* Optimal disturbances and receptivity in three-dimensional boundary layers. In *Proc. 5th European Conference on Computational Fluid Dynamics ECCOMAS CFD* (ed. J. C. F. Pereira & A. Sequeira) Lisbon, Portugal, 14–17 June 2010.

TEMPELMANN, D., HANIFI, A. & HENNINGSON, D. S. 2010*b* Spatial optimal growth in three-dimensional boundary layers. *J. Fluid Mech.* **646**, 5–37.

https://doi.org/10.1017/jfm.2012.235 Published online by Cambridge University Press

TING, L. 1965 On the initial conditions for boundary layer equations. *J. Math. Phys.* **44**, 353–367.

TREFETHEN, L. N., TREFETHEN, A. E., REDDY, S. C. & DRISCOLL, T. A. 1993 Hydrodynamic stability without eigenvalues. *Science* **261**, 578–584.

TUMIN, A. & RESHOTKO, E. 2001 Spatial theory of optimal disturbances in boundary layers. *Phys. Fluids* **13** (7).

TUMIN, A. & RESHOTKO, E. 2003 Optimal disturbances in compressible boundary layers. *AIAA Paper* 2003-0792.

WEIDEMAN, J. A. & REDDY, S. C. 2000 A MATLAB differentiation matrix suite. *ACM Trans. Math. Softw. (TOMS)* **26** (4).

ZUCCHER, S., TUMIN, A. & RESHOTKO, E. 2006 Parabolic approach to optimal perturbations in compressible boundary layers. *J. Fluid Mech.* **556**, 189–216.

ZURIGAT, Y. H., NAYFEH, A. H. & MASAD, J. A. 1990 Effect of pressure gradient on the stability of compressible boundary layers. *AIAA Paper* 90-1451.

https://doi.org/10.1017/jfm.2012.235 Published online by Cambridge University Press